1 # Comparative Study of Strongly and Weakly Coupled Data Assimilation

2 # with a Global Land-Atmosphere Coupled Model

4 Kenta Kurosawa [a,b], Shunji Kotsuki [a,c,d,e,f], and Takemasa Miyoshi [a,b,e,f,g]

5 [a] *RIKEN Center for Computational Science, Kobe, Japan*

6 [b] *Department of Atmospheric and Oceanic Science, University of Maryland, College Park, Maryland, USA*

7 [c] *Center for Center for Environmental Remote Sensing, Chiba University, Chiba, Japan*

8 [d] *PRESTO, Japan Science and Technology Agency, Chiba, Japan*

9 [e] *RIKEN interdisciplinary Theoretical and Mathematical Sciences Program, Kobe, Japan*

10 [f] *RIKEN Cluster for Pioneering Research, Kobe, Japan*

11 [g] *Japan Agency for Marine-Earth Science and Technology, Yokohama, Japan*

13 *Corresponding author*: Kenta Kurosawa (kkurosaw@umd.edu), Shunji Kotsuki

14 (shunji.kotsuki@chiba-u.jp)

16   ABSTRACT

17   This study explores coupled land-atmosphere data assimilation (DA) for improving

18   weather and hydrological forecasts by assimilating soil moisture (SM) data. This study

19   integrates a land DA component into a global atmospheric DA system of the Nonhydrostatic

20   ICosahedral Atmospheric Model and the Local Ensemble Transform Kalman Filter and

21   performs both strongly and weakly coupled land-atmosphere DA experiments. We explore

22   various types of coupled DA experiments by assimilating atmospheric observations and SM

23   data simultaneously. The results show that analyzing atmospheric variables by assimilating SM

24   data improves the SM analysis and forecasts and mitigates a warm bias in the lower troposphere

25   where a dry SM bias exists. On the other hand, updating SM by assimilating atmospheric

26   observations has detrimental impacts due to spurious error correlations between the

27   atmospheric observations and land model variables. We also find that assimilating SM by

28   strongly coupled DA is beneficial in the Sahel and equatorial Africa from May to October.

29   These regions are characterized by seasonal variations in the precipitation patterns and benefit

30   from updates in the atmospheric variables through SM DA during periods of increased

31   precipitation. Additionally, these regions coincide with those identified in the previous studies,

32   where a global initialization of SM would enhance the prediction skill of seasonal precipitation.

33   **1. Introduction**

34   The Earth's natural environment can be considered a unified system in which several

35   subsystems (e.g., atmosphere, hydrosphere, cryosphere, and biosphere) interact with each

36   other. Coupled models consider at least two of the Earth's subsystems and have been developed

37   to emulate such interactions within unified systems. For example, coupled land–atmosphere

38   models consider land–atmosphere interactions by passing the output data from the land

39   subsystem to the atmospheric subsystem and vice versa during model time integrations.

40   Coupled models represent more realistic physical processes and provide improved predictions

41   of Earth's phenomena compared to those models that consist of only a single component.

42   Data assimilation (DA) plays an important role in numerical weather prediction (NWP) by

43   providing accurate initial conditions. Some studies investigated coupled DA for ocean–

44   atmosphere interactions (e.g., Zhang et al., 2007; Sugiura et al., 2008; Fujii et al., 2009; Frolov

45   et al., 2016; Laloyaux et al., 2016; Sluka et al., 2016; Browne et al., 2019; Penny and Hamill

46   2017; Penny et al., 2019) and land-atmosphere interactions (e.g., de Rosnay et al., 2012; Lea

47 et al., 2015; Suzuki et al., 2017; Sawada et al., 2018; Draper and Reichle, 2019; Fairbairn et
48 al., 2019).

49   In this study, we focus on experiments to evaluate the potential benefits of assimilating
50 synthetic soil moisture (SM) data from the Global Land Data Assimilation System (GLDAS;
51 Rodell et al., 2004), within a controlled experimental setup through the effective use of land-
52 atmosphere interactions via data assimilation. Specifically, this study investigates whether
53 assimilating atmospheric (land) observational data into land (atmospheric) models is beneficial
54 for their subsequent forecasts. We employ SM data from GLDAS, a comprehensive and
55 reliable dataset which facilitates simple data handling and is suitable and sufficient for this
56 study (cf. Section 2d). SM is particularly important among land variables because it controls
57 the exchange of water and energy between the atmosphere and land surface (Bateni and
58 Entekhabi, 2012). For example, SM has a profound impact on the evolution of boundary layers
59 and precipitation during the warm season, a time characterized by high incoming radiation and
60 evapotranspiration (Betts, 2009; Dirmeyer and Halder, 2016; Drusch and Viterbo, 2007).
61 Moreover, improving SM data is essential for enhancing seasonal-scale climate predictions
62 (Dirmeyer, 2000; Douville and Chauvin, 2000; Drusch, 2007; Hauser et al., 2017). With a
63 regional NWP system, Santanello et al. (2019) showed that SM DA changed surface fluxes,
64 evolution, and entrainment of the planetary boundary layer, and ambient weather.

65   Two well-known coupled DA methods are weakly coupled DA and strongly coupled DA
66 (cf. section 2.b). As one argument, Lawless (2012) noted that strongly coupled DA is preferable
67 for environmental prediction, as discussed at the 2012 International Workshop on Coupled
68 Data Assimilation. A follow-up workshop in Toulouse in 2016 further elaborated on the need
69 for coupled DA. As for ocean-atmosphere models, Penny et al. (2019) explored a method to
70 improve the initialization process using a simplified model. They estimated ocean conditions
71 with atmospheric observations and vice versa, and found strongly coupled DA approaches were
72 generally superior to weakly coupled approaches when using the simple toy model. As Tang
73 et al. (2021) stated, however, regarding more complex models, it is unclear whether strongly
74 coupled DA generally outperforms weakly coupled DA. When it comes to land-atmosphere
75 models, several studies have demonstrated the benefits of strongly coupled DA approaches for
76 medium-range NWP (Suzuki et al., 2017; Sawada et al., 2018). In terms of assimilation of land
77 observations, while weakly coupled land–atmosphere DA is still the mainstream in NWP
78 systems (e.g., Zhang et al., 2007; Lea et al., 2015; Draper and Reichle, 2019), several studies

79   have already examined the benefits of strongly coupled DA on land observations. For example,

80   Lin and Pu (2019, 2020) assimilated surface SM, 2-m temperature and humidity, and

81   conventional atmospheric observations, showing advantages of strongly coupled DA. They

82   also showed that SM had crucial impacts on the temperature field rather than the other

83   variables. Thus, it is already known that SM DA is beneficial for the coupled land-atmosphere

84   models, but updates of cross-components have not yet been explored enough. Therefore, this

85   study aims at exploring better strategies to assimilate SM data in a strongly coupled land-

86   atmosphere DA system.

87   This study uses a global atmospheric DA system known as the NICAM-LETKF (Terasaki

88   et al., 2015), which consists of the Nonhydrostatic Icosahedral Atmospheric Model (NICAM;

89   Satoh et al., 2008, 2014) and the Local Ensemble Transform Kalman Filter (LETKF; Hunt et

90   al., 2007). NICAM incorporates the Minimal Advanced Treatments of Surface Interaction and

91   RunOff model (MATSIRO; Takata et al., 2003) as the land surface subsystem. We implement

92   coupled land–atmosphere DA in NICAM-LETKF to assimilate SM observations using either

93   the weakly or strongly coupled DA methods. Our primary scientific question is whether the

94   assimilation of synthetic observational data from one model into another can improve

95   compatibility between the two models in the NICAM-LETKF system. In addition to

96   conventional atmospheric observations and AMSU-A radiances in NICAM-LETKF, this study

97   assimilates SM data as land observations.

98   This article is organized as follows. Section 2 describes the newly developed coupled land–

99   atmosphere DA system. The experimental settings are described in Sec. 3. The results are

100 presented and discussed in Sec. 4. Finally, a summary is provided in Sec. 5.

2. Methodology

a. NICAM and MATSIRO models

103   NICAM is an icosahedral-grid-based atmospheric model that has been widely used for

104 NWP (e.g., Kotsuki et al., 2019b, 2019c) and climate-scale predictions (e.g., Kodama et al.,

105 2015; Kikuchi et al., 2017). We use NICAM with a 112-km horizontal resolution and 38

106 vertical layers to a height of approximately 40 km. Due to the relatively coarse horizontal

107 resolution, the Arakawa and Schubert scheme (Arakawa and Schubert, 1974) and Berry's

108 parameterization (Berry, 1967) are employed for cumulus parameterization and the large-scale

109   condensation scheme, respectively. See Satoh et al. (2008) and Satoh et al. (2014) for further
110   details about NICAM.

111   MATSIRO represents all the major processes of water and energy exchange between land
112   and atmosphere. MATSIRO consists of five vertical layers used for simulating soil temperature
113   and moisture: 0−0.05, 0.05−0.25, 0.25−0.5, 0.5−0.75, and 0.75−2 meters. Surface energy and
114   water fluxes are computed from their budgets at the ground and canopy surfaces in snow-free
115   and snow-covered regions, considering the subgrid-scale snow distribution (Takata et al.,
116   2003). SM is calculated in each soil layer and is representative of the entire land component of
117   a model grid area, whether snow-covered or not. Note that, in general, SM in NWP models has
118   been updated using 2-m temperature and humidity observations for decades (e.g. Mahfouf et
119   al., 2000; de Rosnay et al., 2014; Gomez et al., 2020).

120   *b. LETKF and coupled data assimilation implementations*

121   LETKF is a type of ensemble Kalman filter (EnKF; Evensen, 2003) that has been used
122   for atmospheric, hydrological, and oceanic DA. LETKF solves the analysis equations at every
123   model grid point by assimilating the subset of observations within its localization influence
124   radius. The analysis equations of LETKF are based on the ensemble transform Kalman filter
125   (Bishop et al., 2001):

$$\bar{\mathbf{x}}^a = \bar{\mathbf{x}}^f + \delta\mathbf{X}^f\bar{\mathbf{w}}^a, \tag{1}$$

$$\bar{\mathbf{w}}^a = \widetilde{\mathbf{P}}^a(\mathbf{H}\delta\mathbf{X}^f)^{\mathrm{T}}\mathbf{R}^{-1}(\mathbf{y}^o - \mathbf{H}\bar{\mathbf{x}}^f), \tag{2}$$

$$\delta\mathbf{X}^a = \delta\mathbf{X}^f\mathbf{W}^a, \tag{3}$$

$$\mathbf{W}^a = [(m-1)\widetilde{\mathbf{P}}^a]^{\frac{1}{2}}, \tag{4}$$

130   where $\bar{\mathbf{x}}$ is the ensemble-mean model state, $\delta\mathbf{X}$ is the ensemble perturbation matrix, $\mathbf{H}$ is the
131   linear observation operator, $\mathbf{R}$ is the observation error covariance matrix, $\mathbf{y}$ is the observation
132   data, and $\widetilde{\mathbf{P}}^a$ is the model state error covariance matrix in ensemble space, while superscript
133   letters a, f, and o denote analysis (posterior), forecast (prior), and observation, respectively.
134   Here, $\mathbf{P}$ is used for the error covariance in model space, and $\widetilde{\mathbf{P}}$ is used for the error covariance
135   in the ensemble space. m is the ensemble size. $\bar{\mathbf{w}}$ is the ($m \times 1$) ensemble transform vector for
136   the ensemble mean updates, and $\mathbf{W}$ is the ($m \times m$) ensemble transform matrix for ensemble
137   perturbation updates. The analysis error covariance matrix $\widetilde{\mathbf{P}}^a$ is given by

$$\widetilde{\mathbf{P}}^a = [(m-1)\mathbf{I} + (\mathbf{H}\delta\mathbf{X}^f)^{\mathrm{T}}\mathbf{R}^{-1}\mathbf{H}\delta\mathbf{X}^f]^{-1}, \tag{5}$$

139 where $\mathbf{I}$ is the identity matrix. In practice, since the error covariance matrix $\widetilde{\mathbf{P}}^a$ is often

140 underestimated, and filters eventually become unstable, the introduction of the model error or

141 variance inflation is necessary for stable filtering. The theoretical explanation of the model

142 error can partially be attributed to the model nonlinearity under the perfect model assumption.

143 In this study, instead of adding random noise as the model error, we use a relaxation method at

144 the end of the DA process, as described in section 3.

145   The analysis equation of the ensemble mean (Eqs. 1 and 2) is equivalent to the original

146 analysis equation of the Kalman filter:

147
$$\bar{\mathbf{x}}^a = \bar{\mathbf{x}}^f + \delta\mathbf{X}^f\widetilde{\mathbf{P}}^a(\mathbf{H}\delta\mathbf{X}^f)^{\mathrm{T}}\mathbf{R}^{-1}(\mathbf{y}^o - \mathbf{H}\bar{\mathbf{x}}^f)$$

148
$$= \bar{\mathbf{x}}^f + \mathbf{P}^f\mathbf{H}^{\mathrm{T}}(\mathbf{H}\mathbf{P}^f\mathbf{H}^{\mathrm{T}} + \mathbf{R})^{-1}(\mathbf{y}^o - \mathbf{H}\bar{\mathbf{x}}^f). \tag{6}$$

149 Here, $\mathbf{P}^f$ is the model state error covariance matrix in model space. The EnKF uses an

150 ensemble-based approximation to the forecast error covariance:

151
$$\mathbf{P}^f \approx \frac{1}{m-1}\delta\mathbf{X}^f(\delta\mathbf{X}^f)^{\mathrm{T}}. \tag{7}$$

152 For coupled models, Eq. (7) is approximated by

153
$$(\mathbf{P}^f)_{\alpha\beta} \approx \frac{1}{m-1}\delta\mathbf{X}_{\alpha}^f(\delta\mathbf{X}_{\beta}^f)^{\mathrm{T}}, \tag{8}$$

154 where α and β are the model variables updated in the coupled DA. Thus, for coupled land–

155 atmosphere models, $\mathbf{P}^f$ is represented by:

156
$$\mathbf{P}^f = \begin{pmatrix} (\mathbf{P}^f)_{\mathrm{AA}} & (\mathbf{P}^f)_{\mathrm{AL}} \\ (\mathbf{P}^f)_{\mathrm{LA}} & (\mathbf{P}^f)_{\mathrm{LL}} \end{pmatrix}. \tag{9}$$

157 In Eq. (9), 'A' and 'L' represent the variables of the atmosphere and land, respectively. In the

158 current study, for example, $(\mathbf{P}^f)_{\mathrm{AA}}$ represents the covariance between atmospheric variables,

159 and $(\mathbf{P}^f)_{\mathrm{AL}}$ represents that between atmospheric variables and SM. This study employs the

160 ensemble-based estimation of cross-component error covariance ($(\mathbf{P}^f)_{\mathrm{AL}}$ and $(\mathbf{P}^f)_{\mathrm{LA}}$) using

161 Eq. (8). Here each ensemble member represents a coupled forecast where the atmospheric and

162 land variables interact each other. Specifically, the MATSHIRO variables are driven by forcing

163 from NICAM, and the upward flux from MATSHIRO feeds back into NICAM. This coupling

164 captures the essential interactions between the atmosphere and land variable, leading to

165 physically derived cross-component error covariance during the forecasts. Note that the state

166 variable $\mathbf{x}^f$ does not include the land component when the land variables are not updated (cf.

File generated with AMS Word template 2.0

167 Figs. 2 a and d). For such cases, the forecast error covariance matrix also has the inverse matrix
168 since the land component is also excluded in the background error covariance.

169 In practice, since some observations have nonlinear observation operators, the following
170 approximation is required:

$$\mathbf{H}\delta\mathbf{X}^f \approx H\left(\overline{\mathbf{x}}^f\mathbf{1}^{\mathbf{T}} + \delta\mathbf{X}^f\right) - \overline{H\left(\overline{\mathbf{x}}^f\mathbf{1}^{\mathbf{T}} + \delta\mathbf{X}^f\right)}\mathbf{1}^{\mathbf{T}}, \tag{10}$$

172 where H is the nonlinear observation operator, and $\mathbf{1}$ denotes a column vector with all m
173 elements being equal to 1.

174 For the weakly coupled DA (hereafter, WCDA) method, atmospheric observations are
175 used only for updating NICAM state variables, and land observations are used for those of
176 MATSIRO (Fig. 1a). That is, the cross-component error covariance between atmospheric and
177 land variables is assumed to be 0 in WCDA (i.e., $(\mathbf{P}^f)_{AL} = 0$ and $(\mathbf{P}^f)_{LA} = 0$). Thus, impacts
178 of atmospheric observations can propagate to land model states, and vice versa, only through
179 interactions between NICAM and MATSIRO during model forecasts. For the strongly coupled
180 DA (hereafter, SCDA) method, the cross-component covariance is estimated based on
181 ensemble forecasts (i.e., $(\mathbf{P}^f)_{AL} \neq 0$, $(\mathbf{P}^f)_{LA} \neq 0$, or both are nonzero matrices). Therefore,
182 atmospheric or land observations are used to update both NICAM and MATSIRO variables
183 based on the cross-component covariance (Fig. 1b). SCDA extracts more information than
184 WCDA from the same observations if an appropriate forecast error covariance $(\mathbf{P}^f)_{\alpha\beta}$ is
185 applied.
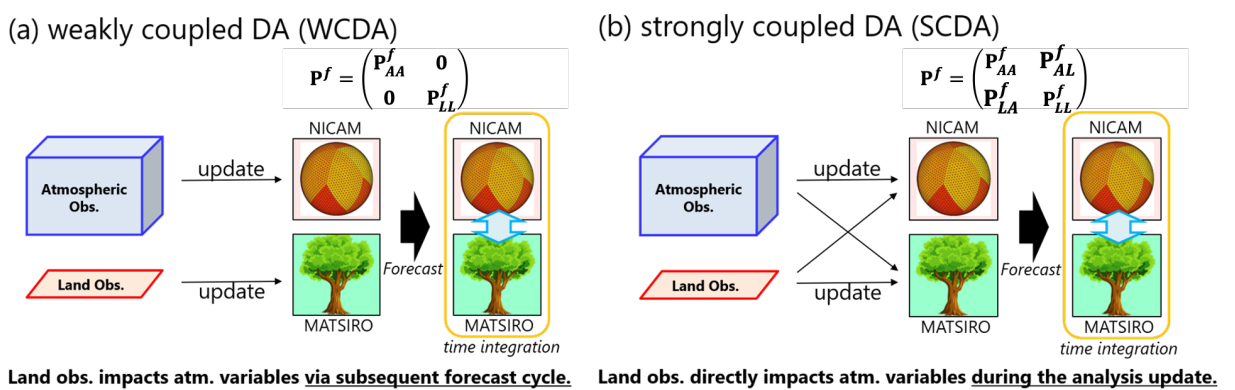
186
187

188 **Figure 1.** Schematic images of (a) weakly coupled and (b) strongly coupled land–
189 atmosphere data assimilation (DA) methods. Thin black arrows indicate model state updates
190 through DA. Cyan double-headed arrows indicate land–atmosphere interactions between

191 NICAM and MATSIRO during subsequent model forecasts. Here, panel (b) shows the full
192 strongly coupled DA method (cf. Fig. 2g). The image for NICAM was adapted from Satoh et
193 al. (2014).

194   This study considers seven coupled DA experiments (Fig. 2). Referring to Penny and
195 Hamill (2017), we classify these experiments into five categories: Quasi-WCDA, WCDA,
196 Quasi-SCDA, SCDA, and Fully SCDA. Here we introduce identifiers (IDs) indicating which
197 observation type is assimilated for each model. This study defines 'A' and 'L' as representations
198 of the atmospheric and land, respectively. The IDs are defined as follows: '$A_{A\times}$' represents that
199 assimilating only atmospheric observations to update the atmospheric model; 'A_{AL}' signifies
200 that assimilating both atmospheric and land observations to update the atmospheric model;
201 '$L_{A\times}$' denotes that assimilating only land observations to update the land model; '$L_{\times L}$' indicates
202 that assimilating only land observations to update the land model; 'L_{AL}' corresponds to that
203 assimilating both atmospheric and land observations to update the land model; finally, '$L_{\times\times}$'
204 represents that no observation is assimilated to update the land model.

205   For example, '$A_{A\times}L_{\times\times}$' indicates that atmospheric observations are used to update the
206 NICAM variables, while no observations are assimilated for the land model (Fig. 2a). This
207 experiment is considered quasi-WCDA and is equivalent to the standard NICAM-LETKF
208 system without SM DA, or the control case (hereafter CTRL). '$A_{A\times}L_{\times L}$' stands for WCDA
209 (Fig. 2b), while '$A_{AL}L_{AL}$' signifies Fully SCDA (hereafter Full-SCDA; Fig. 2g). The remaining
210 four experiments are treated as Quasi-SCDA (Figs. 2c and d) and SCDA (Figs. 2e and f).

211   This study designs specific configurations of SCDA and WCDA to investigate whether
212 updating MATSIRO variables through assimilating particular atmospheric observations has a
213 beneficial impact. This investigation aims at finding the best-performing coupled land-
214 atmosphere DA that consists of updates with a beneficial effect for the experimental setting of
215 the present study. The best-performing approach might be different if we use different DA
216 configurations or change the experimental settings, such as resolution and DA frequency.
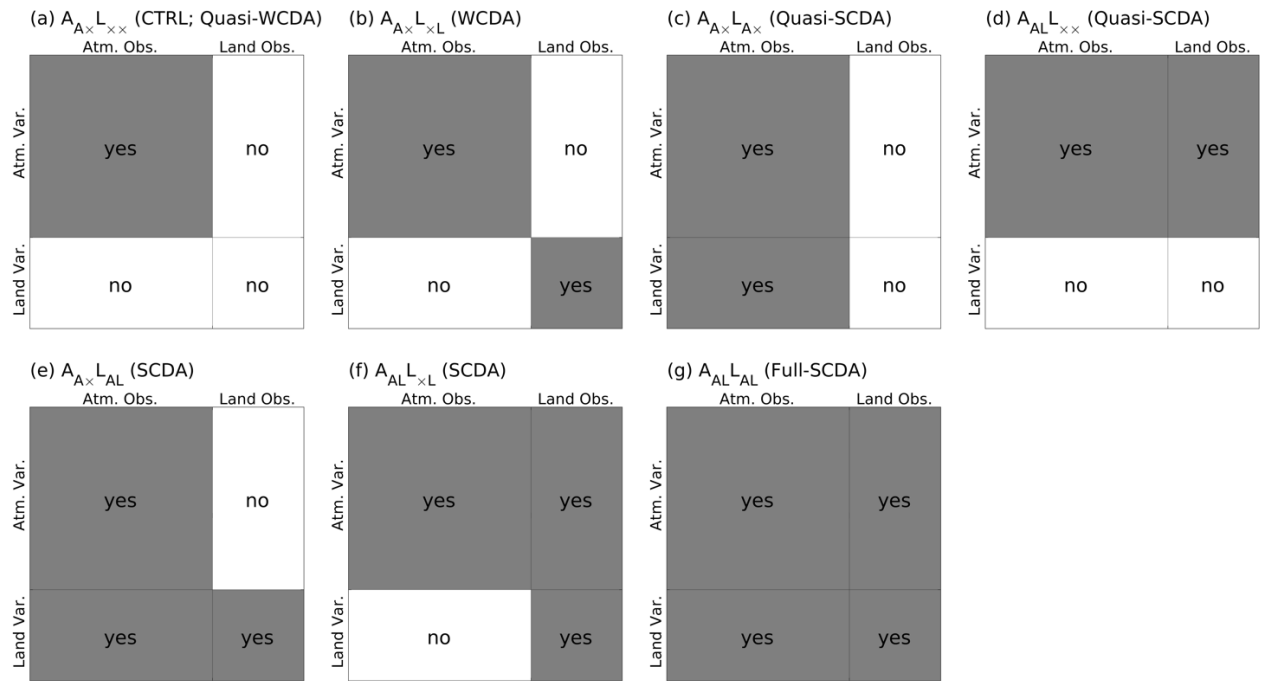
Figure 2. Schematic plots of seven DA experiments for (a) $A_{A\times}L_{\times\times}$ (CTRL; quasi-WCDA), (b) $A_{A\times}L_{\times L}$ (WCDA), (c) $A_{A\times}L_{A\times}$ (quasi-SCDA), (d) $A_{AL}L_{\times\times}$ (quasi-SCDA), (e) $A_{A\times}L_{AL}$ (SCDA), (f) $A_{AL}L_{\times L}$ (SCDA), and (g) $A_{AL}L_{AL}$ (Full-SCDA). The vertical axis represents atmospheric or land variables, and the horizontal axis shows observations. The shading of variables matches that of the observations used for their updates. White areas with 'no' indicate error correlations that are assumed to be zero in DA. Gray areas with 'yes' indicate error correlations that are included in DA.

c. Atmospheric data

The original NICAM-LETKF system assimilates conventional observations from the NCEP operational system (a.k.a. NCEP PREPBUFR), satellite radiance from Advanced Microwave Sounding Unit-A (AMSU-A), and the near-real-time version of Global Satellite Mapping of Precipitation (GSMaP_NRT). The data set includes a number of different types of data: radiosondes, wind profilers, aircraft reports, surface pressure, atmospheric motion vectors and surface winds derived from satellite observations. The channel selections for satellite radiances are 6, 7, and 8 for AMSU-A. The stratospheric sensitive channels are not assimilated in this study, considering relatively low top level of the NICAM in this study (40 km). The satellite radiance scans and airmass biases are adaptively estimated and corrected at each data

237 assimilation cycle. This experimental setting followed the operationally running NICAM-
238 LETKF system. In this study, we use these data as atmospheric observations (cf. Table 1 of
239 Kotsuki et al., 2019a). For further details of the assimilation methods used for these
240 observations, we refer readers to previous studies (Terasaki et al., 2015; Kotsuki et al., 2017a;
241 Terasaki and Miyoshi, 2017).

D. Soil moisture data

243   Satellite instruments can measure several land variables, including SM, surface skin
244 temperature, and snow depth. Previous studies have found that land surface models tend to
245 overestimate SM relative to SM data derived from satellite observations (Bindlish et al., 2018).
246 GLDAS also shows larger SM values than satellite-based data (Bi et al., 2016). The significant
247 bias between the model-based estimate and observation is unfavorable for DA. Prior to DA
248 experiments, we compare spatial distributions of climatological SM for NICAM and satellite-
249 based observations from the Soil Moisture and Ocean Salinity (SMOS; https://smos-
250 diss.eo.esa.int/oads/access/) and the Advanced Microwave Scanning Radiometer 2 of Global
251 Change   Observation   Mission   –   Water   (GCOMW/AMSR-2;
252 https://lance.nsstc.nasa.gov/amsr2-science/). We can see that NICAM SM is greatly biased
253 compared to these satellite-based data (Figs. 3a, c, and d). In contrast, the bias of SM in NICAM
254 relative to GLDAS is much smaller than that relative to SMOS and GCOMW/AMSR-2.
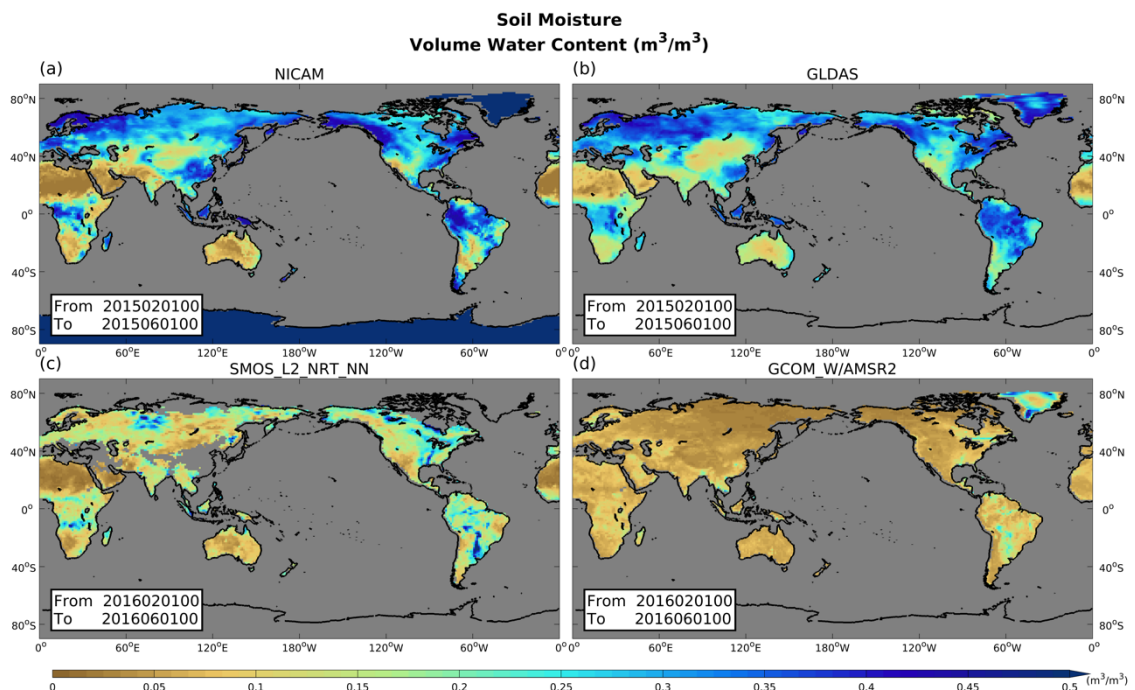
255

256

257   **Figure 3**. Spatial patterns of soil moisture (m^3/m^3) for NICAM, GLDAS,
258   SMOS_L2_NRT_NN, and GCOM_W/AMSR2, averaged over February to June in 2015 (a, b)
259   and 2016 (c, d).

260

261   Hoover and Langland (2017) assimilated pseudo-radiosonde observations from an
262   independent atmospheric reanalysis system. They mentioned that assimilating reanalysis data
263   from an advanced system significantly reduced biases in atmospheric temperature and
264   geopotential height. As a first step, this study takes a similar approach and assimilates SM from
265   GLDAS to avoid using satellite observation data which usually contain significant bias.

266   It is generally known that satellite, remote sensing, and model data sets have different
267   mean SM values. Since we do not know the true mean values in remote sensing or model
268   outputs, we cannot attribute these differences in these mean to bias in any specific data source.
269   Satellite retrieval and model averages are determined by the parameters used in the retrieval
270   and surface models, but we also do not know what those parameters should be. Therefore, the
271   standard approach in SM data assimilation is to remove the difference between modeled and
272   observed SM averages, and then assimilate only the temporal anomalies in the observed SM
273   values. Since it is crucial to have unbiased model and observation states to ensure the DA
274   assumption is correct, several processes are proposed (Dee, 2005). For example, Reichle and
275   Koster (2004) suggest a simple method to remove strong biases between satellite-based and
276   model-based data, in which they match the cumulative distribution functions (CDF) of the
277   satellite and model data (a.k.a. CDF matching approach). On the other hand, several previous
278   studies have successfully performed data assimilation without bias correction (e.g., De Lannoy
279   et al., 2007; Bosilovich et al., 2007; Reichle et al., 2010; Honda et al., 2018). For example,
280   Honda et al. (2018) demonstrated that assimilating geostationary satellite infrared radiance
281   observations without bias correction every 10 minutes reduced the bias between the forecast
282   and observations, leading to improved analysis without causing inconsistencies in the model
283   states. Following the success of these previous studies, the present study assimilates SM data
284   without bias correction. As shown later in Section 4a, the bias between the forecast and
285   observation becomes negligible after a one-month spin-up period when SM from GLDAS is
286   assimilated every 6 hours. Consequently, assimilating SM data without bias correction yields
287   improvements in prediction accuracy of atmospheric variables. Since employing bias

File generated with AMS Word template 2.0

288 correction techniques and assimilating real satellite-sensed SM data could potentially lead to
289 further enhancements, such endeavors are important subjects for future studies.

290 We perform QC using flags provided with the satellite observation data. In addition, as
291 applied for PREPBUFR and GSMaP_NRT observations, we simply apply a gross error check
292 for SM in which observations are rejected when the observation-minus-forecast value is greater
293 than 10 times the observation error standard deviation (Terasaki et al. 2015).

294 GLDAS is a research-oriented land surface reanalysis system that produces
295 spatiotemporally continuous global SM data. The GLDAS system integrates a suite of land
296 surface models, which include the Noah, Community Land Model, Variable Infiltration
297 Capacity, Mosaic, and Catchment. These land surface models provide physically-based
298 simulations of surface conditions, and each model has strengths and weaknesses depending on
299 the applications. Among them, this study uses Noah model-based SM data (GLDAS Noah Land
300 Surface Model L4 Version 2.1; Chen et al., 1996; Koren et al., 1999). We assimilate only first-
301 layer SM since satellite measurements cannot observe deep-layer SM. GLDAS provides 3-
302 hourly SM at a spatial resolution of $0.25^{\circ} \times 0.25^{\circ}$. As these data are denser than those of
303 NICAM (112-km and 6-hourly resolution), we reduce the data density spatially and temporally.
304 The original SM data are averaged within a NICAM model grid so that each observation
305 corresponds to one model grid point. The original 3-hourly data are also averaged over 6 hours.
306 These spatial and temporal data aggregation processes are carried out simultaneously prior to
307 data assimilation.

308 The GLDAS Version 2.1 simulation is forced with National Oceanic and Atmospheric
309 Administration (NOAA)/ Global Data Assimilation System (GDAS) atmospheric analysis
310 fields (Derber et al., 1991), the disaggregated Global Precipitation Climatology Project (GPCP)
311 V1.3 Daily Analysis precipitation fields, and the Air Force Weather Agency's AGRicultural
312 METeorological modeling system (AGRMET) radiation fields. Because GLDAS uses
313 observed precipitation of GPCP, SM in GLDAS is considered better than that of MATSIRO,
314 which uses precipitation forecasts from NICAM to drive the land surface model. Since SM in
315 NICAM has a large bias against the satellite-based product (Fig. 3), this study assimilates SM
316 from GLDAS as pseudo-observations as Hoover and Langland (2017) and verifies forecasted
317 SM compared to GLDAS.

318

3. Experimental setting

This study performs 40-member NICAM-LETKF experiments. NICAM ensemble forecasts are performed for 9-hour intervals, and observation data from the last 6-hour period are assimilated. The initial ensemble members of the experiments are obtained from the 1st-40th members of a long-term 128-member NICAM-LETKF experiment (Terasaki et al. 2019). This means the initial ensemble spread of SM relies on initial conditions perturbed by the ensemble NICAM forecasts. Covariance localization in LETKF is applied to the observation error covariance **R** so that distant observations have smaller impacts on the analysis (Hunt et al., 2007; Miyoshi and Yamane, 2007). Gaussian functions are used for horizontal and vertical localization, given by:

$$f = \exp\left[-\tfrac{1}{2}\{(d_h/\sigma_h)^2 + (d_v/\sigma_v)^2\}\right], \qquad (11)$$

where f is the localization function and d_h and d_v are the horizontal distance (km) and vertical difference (log(Ps)) between the analysis model grid point and the observation, respectively. Standard deviations (SDs) σ_h and σ_v are 400 km and 0.4 natural log pressure as Terasaki et al. (2019) implemented. The localization function is replaced by zero beyond $2\sqrt{10/3}\cdot\sigma_{h,v}$. Land (atmospheric) observations are assimilated into the atmospheric (land) model using the same vertical localization scale. For land observations, surface pressure (Ps) is assigned for the observed height. This study uses relaxation to prior spread (RTPS; Whitaker and Hamill, 2012) for covariance inflation. For atmospheric variables, the relaxation parameter is set to 0.90, which is determined through sensitivity tests (Kotsuki et al., 2017b). As mentioned in Sec. 2 b, the original NICAM-LETKF method, which assimilates only atmospheric observations, is referred to as the control experiment. These experimental settings have been widely applied in previous NICAM-LETKF experiments (e.g., Kotsuki et al., 2018, 2019a). In addition to atmospheric observations, this study assimilates SM data as hydrological land observations. The observation error SD of SM is estimated at 0.05 (m³ m⁻³) based on the innovation statistics of Desroziers (2005) (cf. appendix A). We perform one control experiment and six SM DA experiments, as shown in the schematic images of Fig. 2.

Maintaining the ensemble spread is important in the EnKF. We initially expected that ensemble forecasts could sufficiently maintain the ensemble spreads of MATSIRO variables due to physical coupling with NICAM. However, the ensemble spread of SM in MATSIRO decreased rapidly after initiating assimilation of SM from GLDAS in our preliminary

350 experiment (not shown). We were unable to mitigate this rapid reduction of ensemble spreads
351 even by applying RTPS with relaxation parameter α=0.90. This outcome seems to be related
352 to two fundamental challenges: (1) the land models are typically more dependent on external
353 forcing, rather than being modeled as a chaotic dynamical system dependent on initial
354 conditions, and (2) the timescales for dynamical changes in land models are much longer than
355 those in atmospheric models. The latter implies that the land model is likely to have a long
356 memory beyond 6 hours for SM. In the case of assimilating SM with atmosphere-land coupled
357 models, SM observations correspond to the slow mode, and atmospheric variables correspond
358 to the fast mode. Therefore, offline land DA systems usually inflate the ensemble spread by
359 adding random noise to atmospheric forcing or observational data. For example, Reichle et al.
360 (2002) added perturbations to the ensemble forecasting system, specifically to forcing and to
361 the model states variables, to account for sources of model error in the land model forecast to
362 generate an ensemble representative of the model forecast uncertainty. In the current study, we
363 use RTPS to maintain the ensemble spread of SM in MATSIRO to avoid the ensemble
364 becoming too confident. In addition, land DA experiments with the land-atmosphere system
365 would represent model errors to some extent since each land model is driven by different
366 forcing. The relaxation parameter for SM is set to α=1.00 so that the analysis ensemble spread
367 is equivalent to the forecast ensemble spread. For further details on creating ensemble spreads
368 for land models, we encourage readers to review the summary presented in Draper (2021).

369   Further, since satellite-borne microwave sensors can measure only surface layer SM,
370 we explore better DA strategies that will be applicable to satellite observations. Thus, we only
371 use SM data in the surface layer (0-0.1 meters) provided by GLDAS. In our experiments,
372 GLDAS SM data are assimilated into the topmost layer of MATSIRO (0−0.05 meters).
373 Although analyzing deeper layers of SM is essential to take advantage of land-atmosphere
374 coupling, this study focuses on the surface layer where feedbacks to the atmosphere would be
375 more pronounced than in deeper layers. Note that the present experimental setting for
376 assimilating GLDAS SM data may result in more significant impacts than the experiments with
377 actual satellite observation intervals.

378   We first perform a spin-up NICAM-LETKF experiment from June to September 2014
379 by assimilating only atmospheric observations. The initial NICAM ensemble conditions are
380 taken from the long-term NICAM-LETKF experiment of Terasaki et al. (2019). DA
381 experiments are performed for 13 months, from 0000 UTC 1 October 2014 to 1800 UTC 30

382   November 2015. The first month (October 2014) is considered as a spin-up period, and the

383   results for the latter 12 months are used for validation.

384   In Sec. 4 a, the data are used for validation to check if the assimilation behaves as

385   expected (i.e., the analysis departures of SM are reduced by the assimilation). In addition, we

386   also use SM from ERA5 reanalysis data (Hersbach et al., 2020) as an independent dataset for

387   validation scores. We evaluate atmospheric variables against the ERA5 reanalysis data in Sec.

388   4 b. The analysis of land variables is performed separately from the atmospheric analysis in

389   the ERA5 by assimilating screen-level temperature, dewpoint, and synoptic observations with

390   the optimal interpolation. While the ERA5 assimilates no SM observation, the ERA5

391   assimilates many more satellite observations than the NICAM-LETKF, such as Microwave

392   Humidity Sounder and Advanced Technology Microwave Sounder. Therefore, validating

393   NICAM-LETKF atmospheric fields relative to the ERA5 is reasonable. Furthermore, as

394   described, SM of GLDAS can be considered better than the NICAM-LETKF because it is

395   derived by observed precipitation. Hence, in the following sections, we demonstrate that the

396   assimilation of SM from GLDAS has a beneficial effect on atmospheric fields in NICAM-

397   LETKF, as verified by comparison with ERA5.

398   4. Results and discussion

399   *a. Impacts on soil moisture*

400   We first examine the impacts of SM assimilation on MATSIRO. Figure 4 compares the

401   global bias patterns for the prior state of SM at the near-surface layer (i.e., 0-0.05m) relative to

402   GLDAS, averaged over a 12-months period from November 2014 to October 2015. Three

403   panels show the results for $A_{A\times}L_{\times\times}$ (CTRL; quasi-WCDA), $A_{A\times}L_{\times L}$ (WCDA), and $A_{AL}L_{AL}$

404   (Full-SCDA). $A_{A\times}L_{\times\times}$ (CTRL) shows dry biases relative to GLDAS in general, especially in

405   the continents of Africa, South America, Australia, and Central Eurasia (Fig. 4a). Assimilating

406   SM into MATSIRO successfully mitigates these SM biases (Figs. 4b and c). Furthermore,

407   assimilating SM mitigates the wet SM bias in regions where SM is overestimated in $A_{A\times}L_{\times\times}$

408   (CTRL). Therefore, the newly developed coupled land–atmospheric DA system successfully

409   assimilates SM data into MATSIRO, and we confirm the developed DA system works well.

410   These results are expected and not surprising because forecasts are validated using the same

411   data as observations. No notable differences are observed in global bias patterns between

412     $A_{A\times}L_{\times L}$ (WCDA) and $A_{AL}L_{AL}$ (Full-SCDA) in global bias patterns (Figs. 4b and c).

Mean BIAS
Soil Moisture [m³/m³]
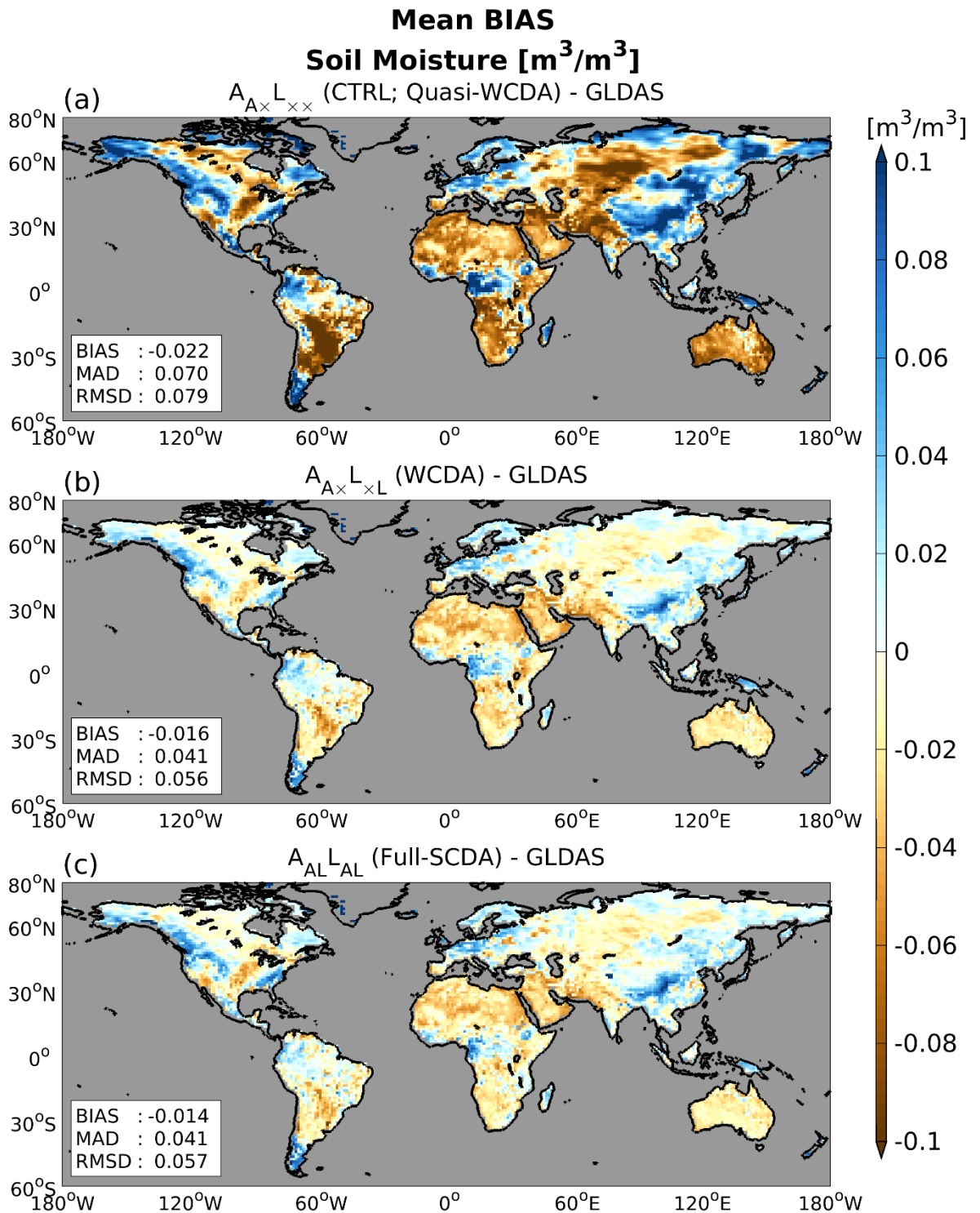
413

414

415   **Figure 4.** Global patterns of 6-hour forecast bias for soil moisture (SM; m³ m⁻³) relative to

416   GLDAS for (a) $A_{A\times}L_{\times\times}$ (CTRL; quasi-WCDA), (b) $A_{A\times}L_{\times L}$ (WCDA), and (c) $A_{AL}L_{AL}$ (Full-

417   SCDA), averaged over 12 months from November 2014 to October 2015. The blue and brown

colors represent overestimated and underestimated SM values relative to GLDAS, respectively.
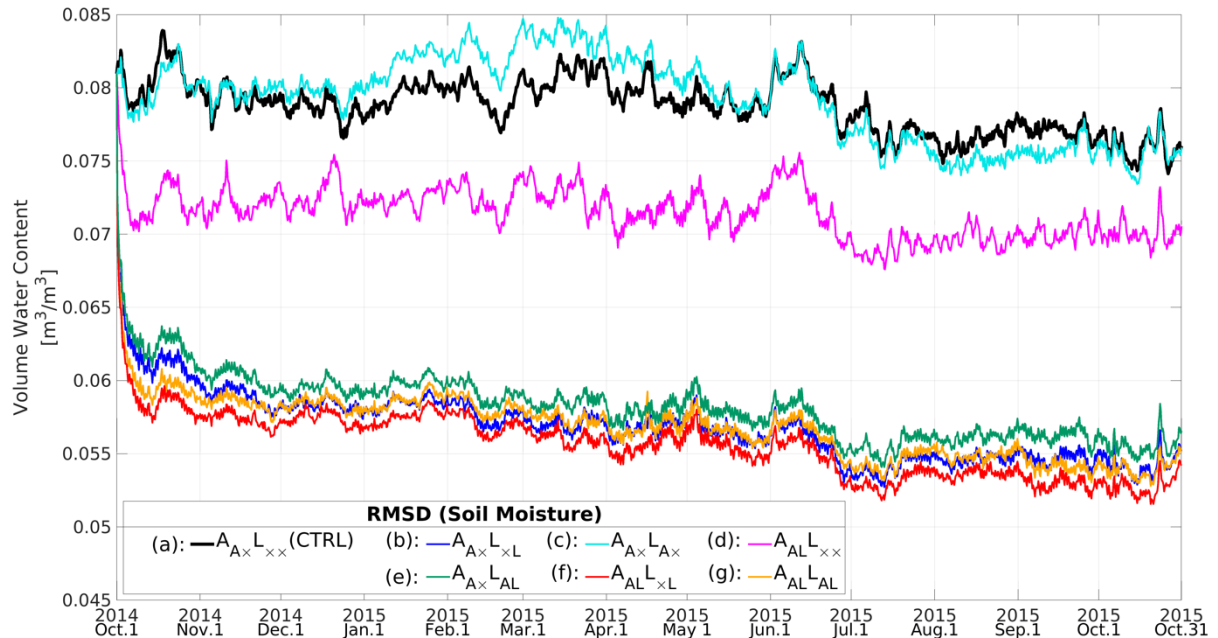
Figure 5. Time series of global-mean forecast root mean square differences (RMSDs) for soil moisture (SM; $m^3 \ m^{-3}$) relative to GLDAS. The black, blue, cyan, magenta, green, red, and yellow lines indicate (a) $A_{A\times}L_{\times\times}$ (CTRL; quasi-WCDA), (b) $A_{A\times}L_{\times L}$ (WCDA), (c) $A_{A\times}L_{A\times}$ (quasi-SCDA), (d) $A_{AL}L_{\times\times}$ (quasi-SCDA), (e) $A_{A\times}L_{AL}$ (SCDA), (f) $A_{AL}L_{\times L}$ (SCDA), and (g) $A_{AL}L_{AL}$ (Full-SCDA) experiments, respectively. Experiments (a)−(g) correspond to the DA patterns (a)−(g) shown in Fig. 2.

Figure 5 shows the time series of global-mean root mean square differences (RMSDs) for SM relative to GLDAS. All experiments that assimilate SM have smaller errors in SM than those in $A_{A\times}L_{\times\times}$ (CTRL; Fig. 5a). Although $A_{A\times}L_{\times L}$ (WCDA; Fig. 5b) and $A_{AL}L_{AL}$ (Full-SCDA; Fig. 5g) show reduced errors, no clear difference is apparent between the two experiments. Among the seven experiments, $A_{AL}L_{\times L}$ (SCDA; Fig. 5f) results in the smallest SM error. In this experiment, SM observations are used for updating both NICAM and MATSIRO, whereas atmospheric observations are used only for updating NICAM and not for MATSIRO. Since $A_{AL}L_{\times L}$ (SCDA) results in better SM estimation than $A_{AL}L_{AL}$ (Full-SCDA;

438 Fig. 5g), we can see that updating SM in MATSIRO through assimilation of atmospheric

439 observations have a detrimental impact on SM in the experimental settings of this study.

440 Such detrimental impacts are also found by comparing other cases, such as $A_{A\times}L_{\times L}$

441 (WCDA; Fig. 5b) and $A_{A\times}L_{AL}$ (SCDA; Fig. 5e). The larger error in $A_{A\times}L_{AL}$ (SCDA) than in

442 $A_{A\times}L_{\times L}$ (WCDA) arises from inaccurate covariance estimates between atmospheric

443 observations and land variables due to insufficient ensemble size. Ensemble-based DA can

444 provide spurious error correlations when the ensemble size is small. Assimilating observations

445 based on spurious error covariances generally degrades the analysis results (cf. variable

446 localization of Kang et al. 2011). Moreover, the difference in timescale between the

447 atmospheric and terrestrial models may have a dominant influence, which could be verified by

448 experiments using a short assimilation window. Such further investigation of the assimilation

449 window is essential for future studies of land-atmosphere coupled DA.

450 $A_{A\times}L_{A\times}$ (quasi-SCDA; Fig. 5c) shows similar RMSDs to those of $A_{A\times}L_{\times\times}$ (CTRL; quasi-

451 WCDA), which implies that atmospheric observations have neither beneficial nor detrimental

452 impacts on updating SM. Because many types of atmospheric observations are assimilated in

453 this study, clarifying impacts of individual observation type is complicated. The results might

454 be changed if we assimilate only one kind of atmospheric observation, such as precipitation

455 data, with the variable localization. Accurate estimation of $(\mathbf{P}^f)_{AL}$ by increasing the number

456 of ensembles might reduce the RMSD of $A_{A\times}L_{A\times}$ (quasi-SCDA). Penny et al. (2019) also faced

457 this kind of problem when assimilating slower ocean observation data into an atmosphere-

458 ocean model with coupled DA. Penny et al. (2019) found that it was more difficult to use slow-

459 mode observations (from the ocean) to update the fast-mode (atmosphere). They overcame this

460 problem by using larger ensembles and increasing the analysis update and observation

461 frequency. As discussed for maintaining ensemble spreads for SM, SM observations

462 correspond to the slow mode and atmospheric variables correspond to the fast mode in our

463 experimental settings. Therefore, applying Penny et al. (2019)'s approach may further improve

464 SCDA.

465 We can say that Fig. 5 represents the error correlation between the SM observations

466 and the atmospheric model variables, showing that it is more reliable than the correlation

467 between the atmospheric observations and the SM variable from the land model. In terms of

468 reducing the errors in SM, the optimal coupled DA method in our experimental setting is

469 $A_{AL}L_{\times L}$ (SCDA). The errors in SM can be reduced by updating atmospheric and land variables

470   through the assimilation of SM. Several previous studies have found that it is important to

471   correct the "upstream" dynamics in the coupled system (e.g., by Sluka et al., 2016). In other

472   words, since the atmosphere strongly drives the land via surface forcing, correcting the

473   atmospheric variables would improve forecasts of the coupled land surface model. From the

474   point of view of the land model, the SM can be updated accurately by assimilating the observed

475   SM directly. Attempting to use fast-varying atmospheric observations for updating SM would

476   lead to suboptimal analysis because of the non-perfect ensemble-based error covariance

477   estimate between atmospheric observations and modelled SM. In contrast, the detrimental

478   impacts of updating atmospheric variables by $(\mathbf{P}^f)_{AL}$ cancel out the beneficial impacts of

479   updating SM by $(\mathbf{P}^f)_{LA}$. Therefore, for our model configuration and DA design, $A_{AL}L_{AL}$ (Full-

480   SCDA) is less effective than $A_{AL}L_{\times L}$ (SCDA). This problem might occur because the DA

481   approach degrades the analysis when assimilating atmospheric data into the land model. The

482   approaches for atmosphere-ocean coupled DA suggested by Penny et al. (2019) could solve

483   the problem, which will be an important future subject to improve SCDA even more.

484   Figure 6 shows the time series of ensemble spread of SM. Since RTPS is used with a

485   relaxation parameter of 1.0 for land variables, the ensemble spread does not change during DA.

486   Because no significant difference is observed in the ensemble spreads among experiments, the

487   difference in RMSDs relative to GLDAS must originate from the difference in the update

488   strategy. The ensemble spread of $A_{A\times}L_{A\times}$ (quasi-SCDA; Fig. 6c) is the smallest among these

489   cases, which means the atmospheric observations have collapsed the spread more than any

490   other configurations. By assimilating the atmospheric observations into the land model, the

491   impact of the land observations becomes less, leading to the detrimental effect observed in

492   those cases. This could also be related to the balance between the errors on the atmospheric

493   observations and the spread of the land model variables. This indicates that the atmospheric

494   observation error should be inflated when applied to the land DA via SCDA. The process filters

495   out the impact of high variability in the atmosphere, similar to adding errors of

496   representativeness in the spatial dimension.

497
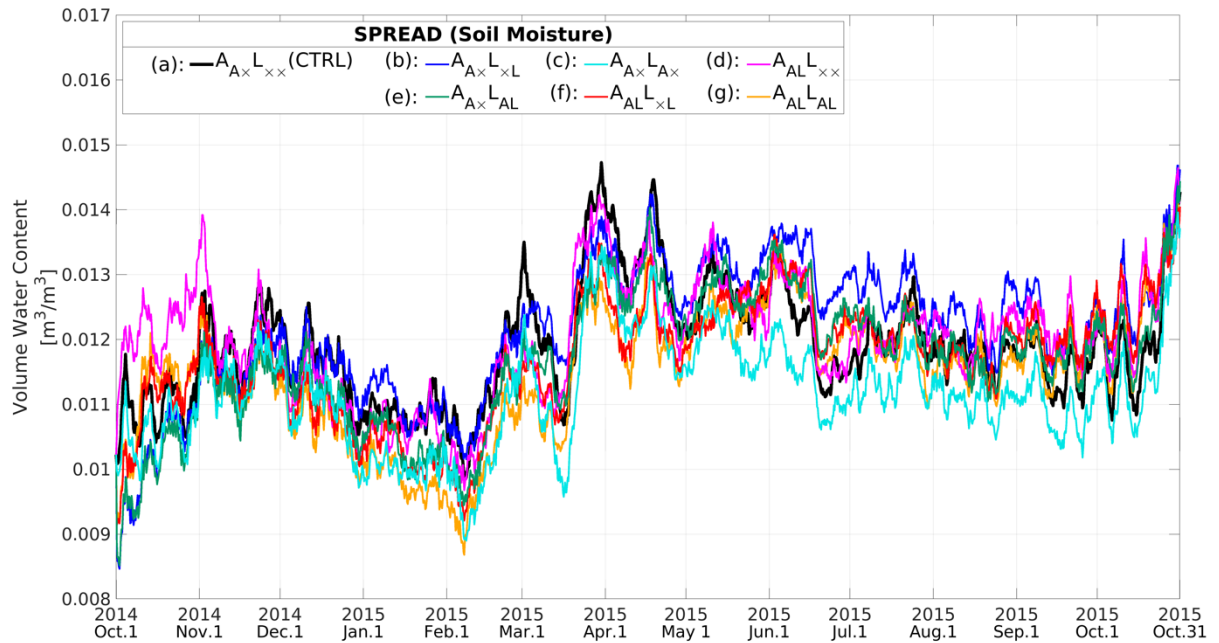
498

499   **Figure 6.** Similar to Fig. 5, but showing forecast ensemble spreads of SM ($m^3 \, m^{-3}$).

500

501   Figure 7 shows the global patterns of differences in analysis RMSDs for SM, averaged
502   over a 12-month period from November 2014 to October 2015. Here, we discuss three
503   experiments: $A_{A\times}L_{\times L}$ (WCDA), $A_{AL}L_{AL}$ (Full-SCDA), and $A_{AL}L_{\times L}$ (SCDA), which are the
504   best three experiments in terms of errors in SM, as shown in Fig. 5. First, we compare $A_{A\times}L_{\times L}$
505   (WCDA) and $A_{AL}L_{\times L}$ (SCDA). Figure 7 (a) suggests that updating atmospheric variables with
506   SM DA generally has beneficial impacts on SM. In South America, the Arabian Peninsula, and
507   India, beneficial impacts are seen in regions where $A_{A\times}L_{\times\times}$ (CTRL) shows a dry bias in SM in
508   Fig. 4. Additionally, beneficial impacts are apparent in Central Africa, where $A_{A\times}L_{\times\times}$ (CTRL)
509   has a wet bias in SM. In contrast, SM DA has moderate impacts in North America and Eurasia.
510   In these areas, $A_{AL}L_{AL}$ (Full-SCDA) performs worse than $A_{A\times}L_{\times L}$ (WCDA; Fig. 7b),
511   suggesting that assimilating atmospheric observations to update SM in MATSIRO would be
512   detrimental in the experimental settings of this study. Therefore, eliminating the updates of
513   MATSIRO with atmospheric observations has beneficial impacts for SCDA (Fig. 7c).

514

Figure 7. Global patterns of soil moisture analysis RMSD (m^3 m^{-3}) relative to GLDAS averaged over 12 months from November 2014 to October 2015: (a) difference between $A_{A \times L} L_{\times L}$ (WCDA) and $A_{AL} L_{\times L}$ (SCDA), (b) difference between $A_{A \times L} L_{\times L}$ (WCDA) and $A_{AL} L_{AL}$ (Full-SCDA), and (c) difference between $A_{AL} L_{AL}$ (Full-SCDA) and $A_{AL} L_{\times L}$ (SCDA). Warm colors indicate that the latter experiments providing smaller scores than the former experiments, whereas cool colors indicate larger scores of the latter methods.

522

523   We also investigate the SM correlations between GLDAS and the results of the

524   experiments (Fig. 8). We can see that the correlation to GLDAS is larger in the regions where

525   positive impacts are observed in Fig. 7. Figure 9 shows the results of the two-sample t-test.

526   Time series of absolute bias of SM analysis relative to GLDAS are sampled from November

527   2014 to October 2015. When the P-values at a point are smaller than 5%, the null hypothesis

528   at the 95% confidence level is rejected, implying a significant difference. By the significance

529   test, we can see the significant differences between the experiments over broad regions. The

530   significant differences between methods $A_{A\times}L_{\times L}$ (WCDA) and $A_{AL}L_{\times L}$ (SCDA) are mainly

531   located in the areas where the bias was relatively substantial in Fig. 4a (Fig. 9a). From Fig. 8

532   and Fig. 9, we can reconfirm the points described in the comments about Fig. 7: (1) using SM

533   to update atmospheric variables has positive effects, especially in areas where there are dry

534   biases, (2) areas where there are wet biases are mitigated by SM DA, and (3) updating SM with

535   atmospheric observations has detrimental effects, leading to the results of $A_{AL}L_{AL}$ (Full-

536   SCDA) experiments.
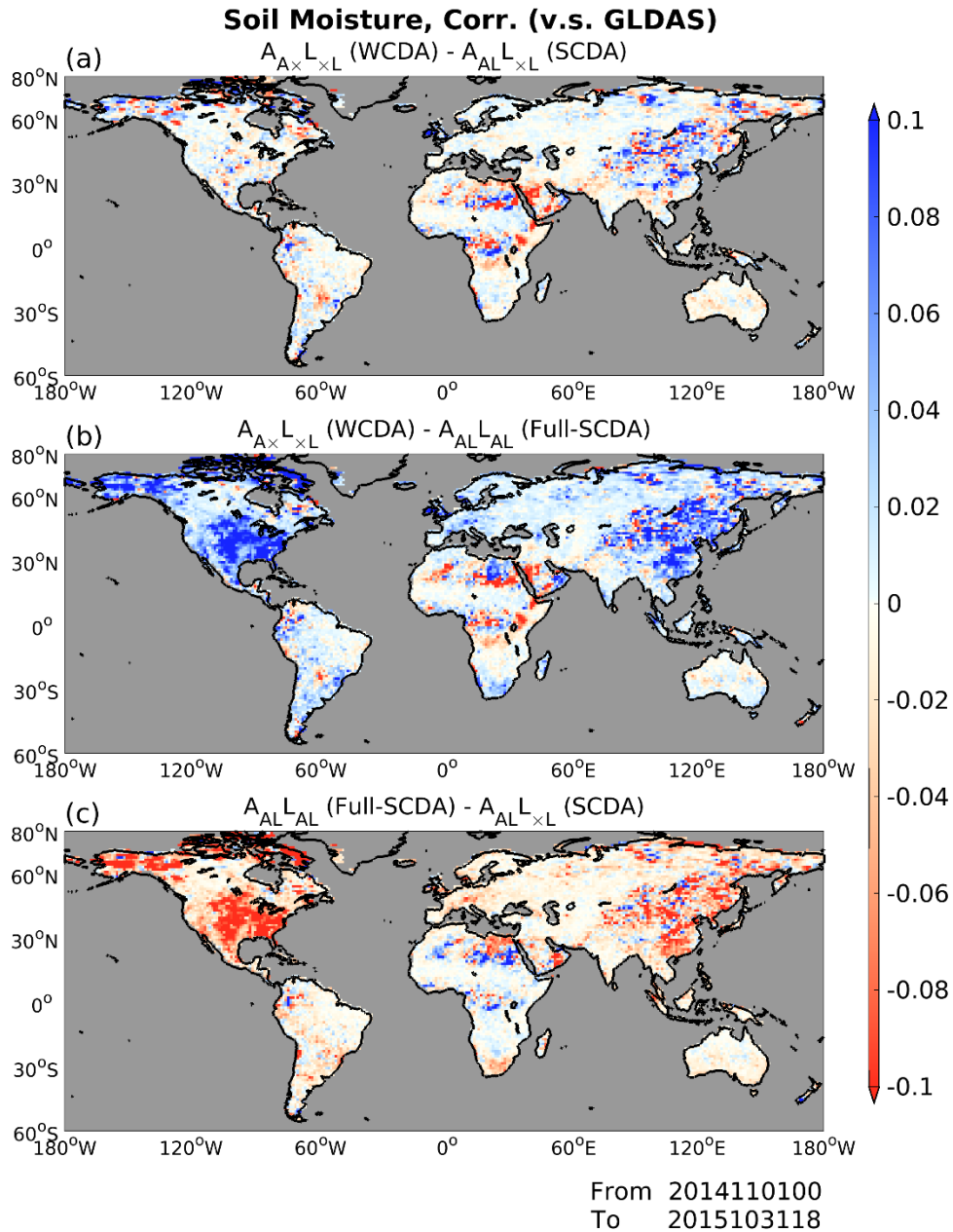
Figure 8. Global patterns of soil moisture analysis correlation relative to GLDAS sampled over 12 months from November 2014 to October 2015: (a) difference between $A_{A\times}L_{\times L}$ (WCDA) and $A_{AL}L_{\times L}$ (SCDA), (b) difference between $A_{A\times}L_{\times L}$ (WCDA) and $A_{AL}L_{AL}$ (Full-SCDA), and (c) difference between $A_{AL}L_{AL}$ (Full-SCDA) and $A_{AL}L_{\times L}$ (SCDA). Warm colors indicate that the latter experiments providing smaller scores than the former experiments, whereas cool colors indicate larger scores of the latter methods.
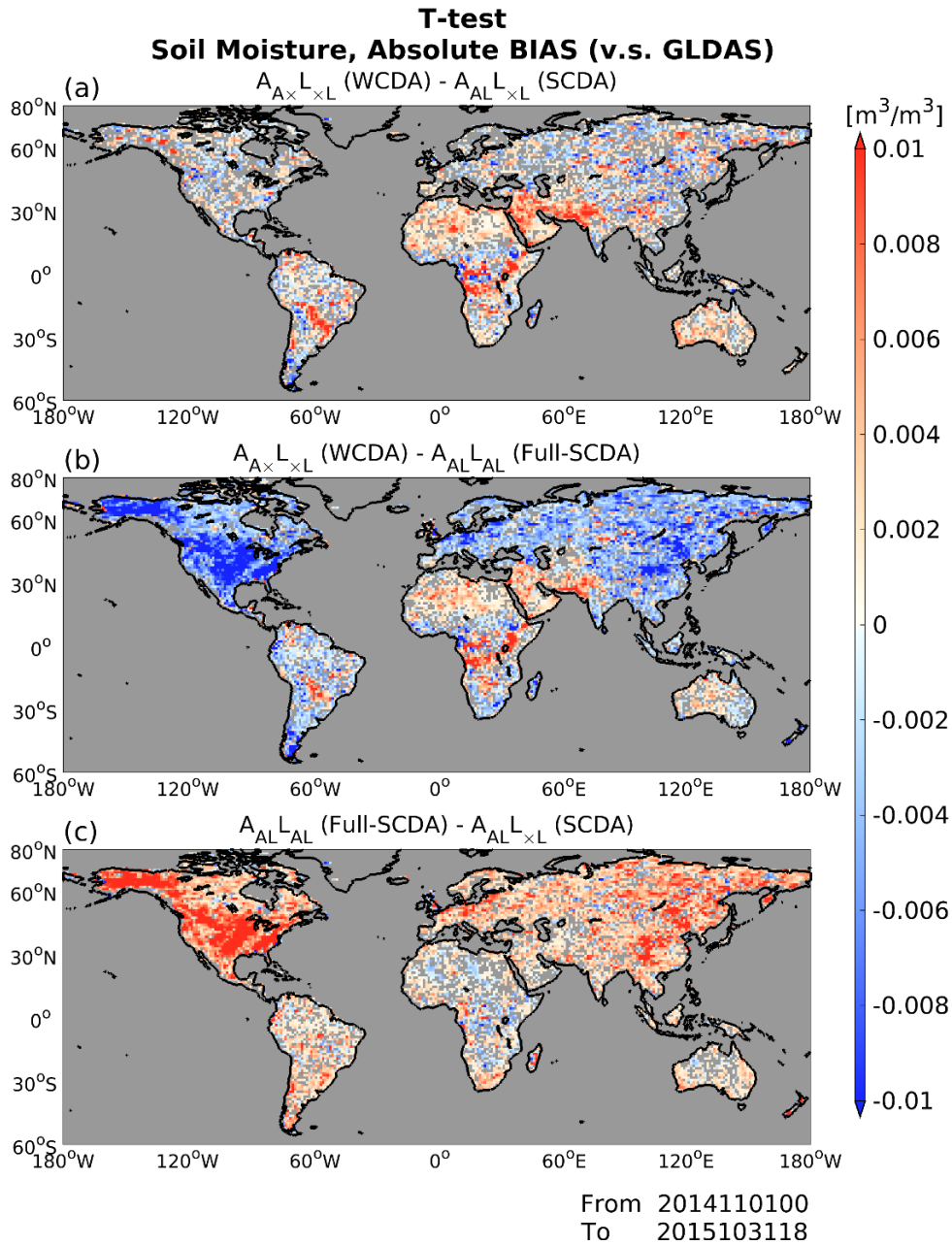
Figure 9. Global patterns of soil moisture analysis absolute bias (m³ m⁻³) relative to GLDAS: (a) difference between $A_{A\times}L_{\times L}$ (WCDA) and $A_{AL}L_{\times L}$ (SCDA), (b) difference between $A_{A\times}L_{\times L}$ (WCDA) and $A_{AL}L_{AL}$ (Full-SCDA), and (c) difference between $A_{AL}L_{AL}$ (Full-SCDA) and $A_{AL}L_{\times L}$ (SCDA). Only the areas where the T-test gives significant differences (the P-value < 5%) are colored, sampling with time series of soil moisture analysis from November 2014 to October 2015. Areas without significant differences are grayed out.

546

547

554

We also investigate the seasonal differences in the relationship between precipitation and SM. Figure 10 compares the difference of SM analysis RMSD relative to GLDAS between $A_{A \times}L_{\times L}$ (WCDA) and $A_{AL}L_{\times L}$ (SCDA; Figs. 10a, c, e, and g), with observed precipitation of GPCP version 1.3 (Figs. 10b, d, f, and h). The SCDA experiment shows improvements in the Sahel and equatorial Africa from May to October (Figs. 10e and g) compared to the period from November to April (Figs. 10a and c). These regions are known to be "hotspots" where SM affects precipitation during June−August (Koster et al. 2004). SM assimilation by SCDA would benefit from updating atmospheric variables in the hotspot regions. On the other hand, the distribution of precipitation from November to April tends to shift slightly southwards, resulting in decreased precipitation in previously defined hotspots (Figs. 10b and d). Therefore, the advantages of updating atmospheric variables using SM data are not as evident in these areas in our experiments (Figs. 10a and c). This period includes the summer season in the Southern Hemisphere. For instance, we can confirm a notable increase in precipitation in South America (Figs. 10b and d). Correspondingly, the advantages of using SCDA in that area become more pronounced. The Arabian Peninsula is another region where the advantages of SCDA stand out during this season, despite being an area with scarce rainfall throughout the year and minimal seasonal differences. Therefore, comparison of results from November to April (Figs. 10a-d) with those from May to October (Figs. 10e-h) implies that the locations of the "hotspots" may vary depending on the season.

From the above results, it is clear that precipitation and SM are closely related. Given the seasonal variation in precipitation distribution, the regions that would benefit from updating atmospheric variables using SM data shift accordingly.

File generated with AMS Word template 2.0
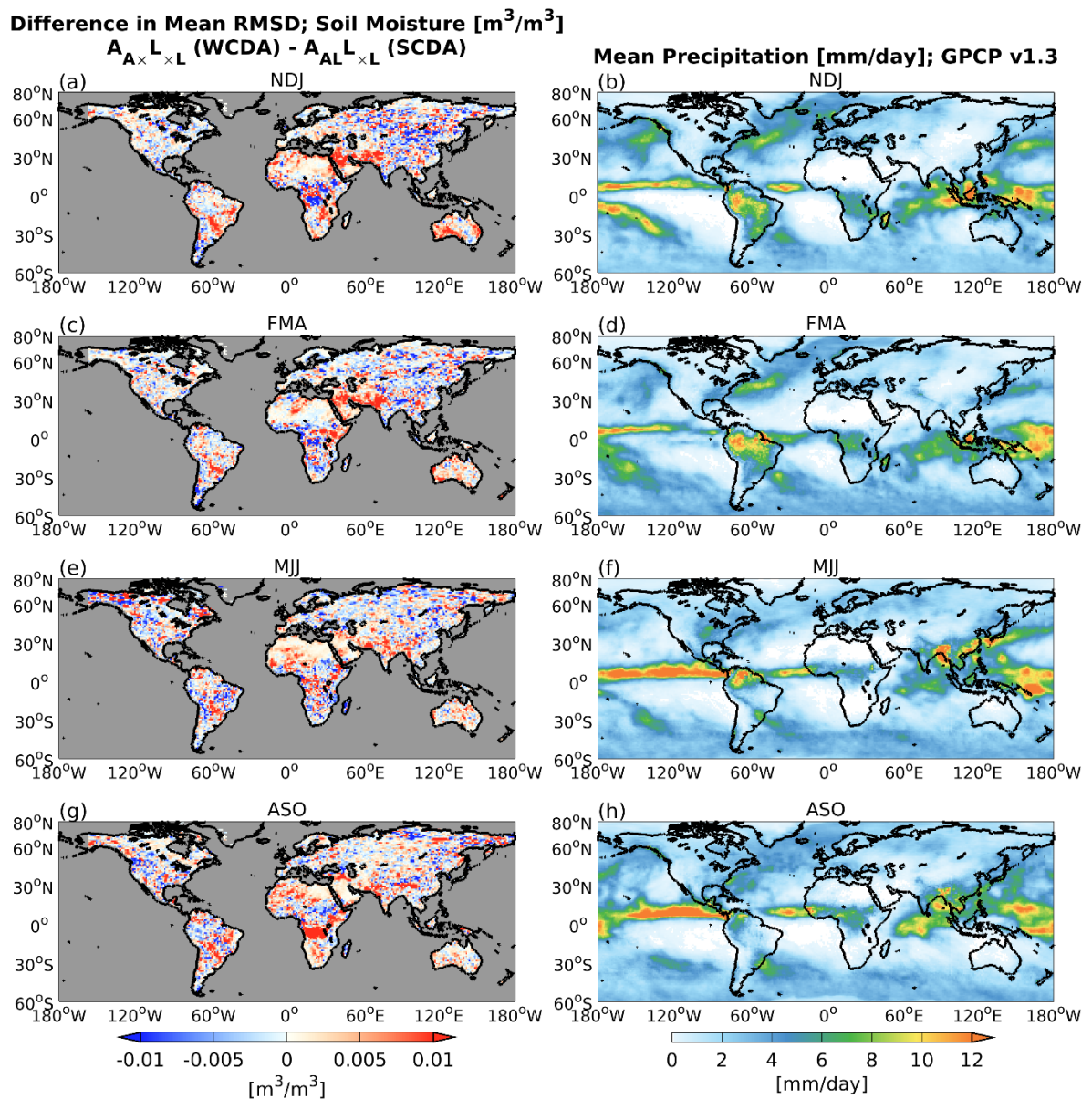
Figure 10. Global patterns of soil moisture analysis RMSD (m^3 m^{-3}) relative to GLDAS (panels a, c, e, g) and spatial patterns of observed precipitation of GPCP version 1.3 (mm/day; panels b, d, f, h). Results are averaged over 3 months: (a, b) November 2014 to January 2015, (c, d) February to April 2015, (e, f) May to July 2015, and (g, h) August to October 2015. Panels (a, c, e, g) show the difference between $A_{A\times}L_{\times L}$ (WCDA) and $A_{AL}L_{\times L}$ (SCDA). In panels (a, c, e, g), warm colors indicate that $A_{AL}L_{\times L}$ (SCDA) performing better than $A_{A\times}L_{\times L}$ (WCDA), whereas cool colors indicate worse performance of $A_{AL}L_{\times L}$ (SCDA).

File generated with AMS Word template 2.0

587   We also use ERA5 SM as an independent dataset for the validation scores, although so far,
588   we have been using GLDAS to verify that the experimental setup works as expected. Fig. 11
589   compares the global patterns of 6-h forecast bias in SM at near-surface layer as in Fig. 4, but
590   relative to ERA5. We can see that $A_{A\times}L_{\times\times}$ (CTRL) shows large dry biases relative to ERA5 in
591   South America and Central Eurasia (Fig. 11a). The dry biases appear mitigated by updating
592   MATSIRO with the SM of GLDAS. Furthermore, NICAM has a large dry bias in the center of
593   the African continent relative to ERA5, which is not the case when compared to GLDAS in
594   Fig. 4. There is a wet bias at the southern and northern ends of the African continent, which
595   increases with the assimilation of SM, but the global-averaged scores show improvements
596   compared to $A_{A\times}L_{\times\times}$ (CTRL; Figs. 11b and c). No notable differences are observed between
597    $A_{A\times}L_{\times L}$ (WCDA) and $A_{AL}L_{AL}$ (Full-SCDA) in global bias patterns (Figs. 11b and c).

598   Figure 12 shows the time series of global-mean RMSDs for SM as in Fig. 5, but relative to
599   ERA5. Similar to the results in Fig. 5, we can find the following features: all experiments that
600   assimilate SM have smaller errors in SM than in $A_{A\times}L_{\times\times}$ (CTRL). $A_{A\times}L_{A\times}$ (quasi-SCDA; Fig.
601   12c) shows larger RMSDs to that of $A_{A\times}L_{\times\times}$ (CTRL) whereas $A_{AL}L_{\times\times}$ (quasi-SCDA; Fig.
602   12d) shows smaller RMSDs than $A_{A\times}L_{\times\times}$ (CTRL). This validation against ERA5 SM also
603   support the previously identified findings: updating atmospheric variables by SM DA is
604   beneficial to improve SM forecasts whereas updating the SM variable by assimilation of
605   atmospheric observations results in detrimental impacts. The differences between the other four
606   experiments, in which SM observations update the MATSIRO variables, are unclear, but they
607   show a significant decrease in RMSDs compared to $A_{A\times}L_{\times\times}$ (CTRL).

608   Lastly, Fig. 13 compares the differences in analysis RMSD of SM relative to ERA5. We
609   can see a meaningful benefit of having atmospheric model variables updated by SM
610   observations where there was a robust dry bias, e.g., in the South American continent (Figs.
611   13a and b). On the other hand, there was originally a wet bias against ERA5, i.e., the Arabian
612   Peninsula and North of the African continent, resulting in a modification effect. Furthermore,
613   a feature not seen in Fig. 7 is that with ERA5 as reference data, there is no significant worsening
614   of the MATSIRO variables by updating them with atmospheric observations (Fig. 13c).

615   The validation results using an independent dataset suggest that the experiments conducted
616   in this study are functioning reasonably well. These findings support the notion that our
617   experiments, which assimilate SM data from GLDAS without bias correction, can perform
618   satisfactorily without violating the underlying assumptions of data assimilation. In this section,

619   the results show that the assimilation of atmospheric observations can lead to detrimental

620   effects on soil moisture analysis. It is crucial to note that this issue stems from the experimental

621   setup rather than statistical aspects. The primary cause of these adverse effects would be the

622   weak dynamical relationship between the lower troposphere and SM. We will explore the

623   issues related to this physical relationship in the subsequent section.

624

Mean BIAS
Soil Moisture [m³/m³]
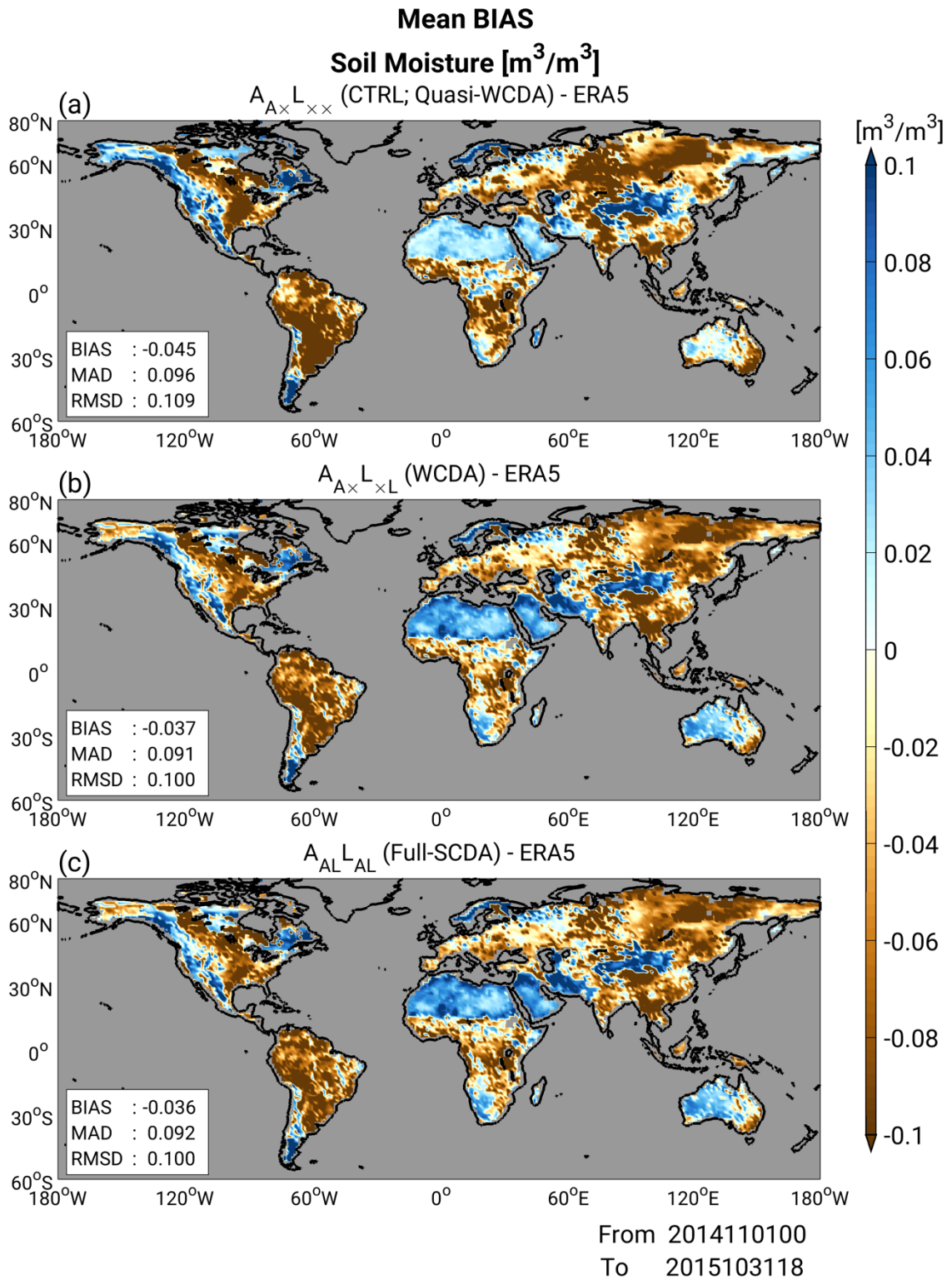
625

626   **Figure 11.** Similar to Fig. 4, but showing 6-hour forecast bias for soil moisture relative to

627   ERA5 (m³ m⁻³).

628
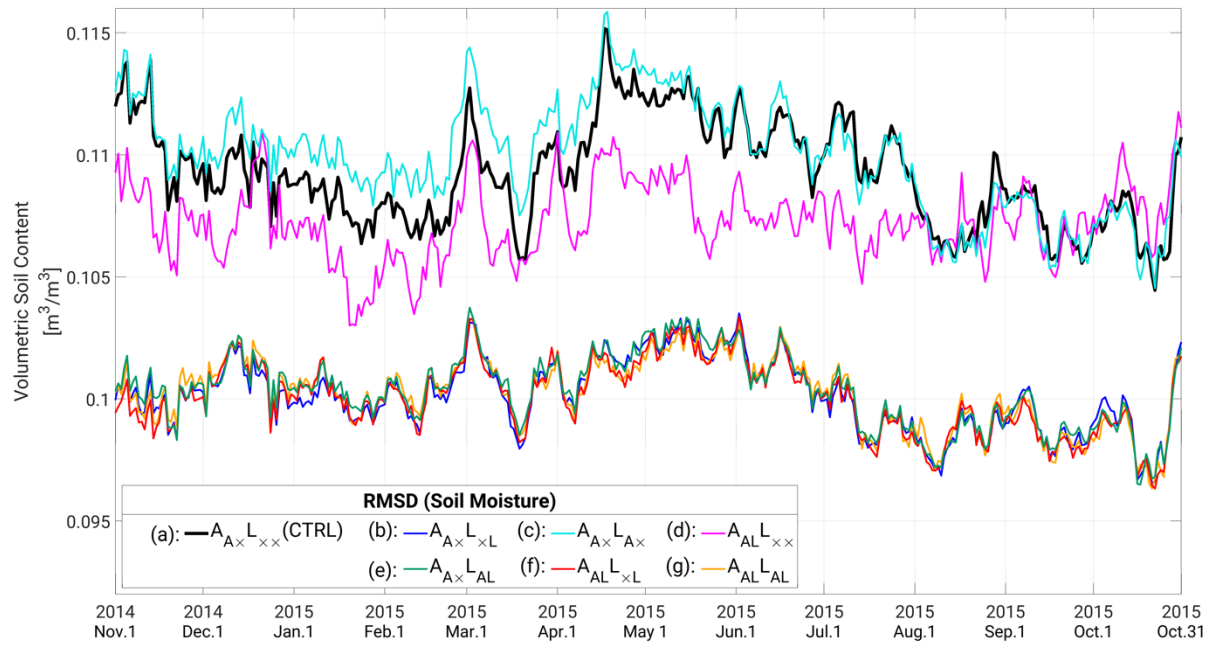
629

630

631   **Figure 12.** Similar to Fig. 5, but showing RMSDs for soil moisture relative to ERA5 (m³
632   m⁻³).

633

Difference in Mean RMSD
Soil Moisture [m³/m³]

(a) $A_{A\times}L_{\times L}$ (WCDA) - $A_{AL}L_{\times L}$ (SCDA)

(b) $A_{A\times L}L_{\times L}$ (WCDA) - $A_{AL}L_{AL}$ (Full-SCDA)

(c) $A_{AL}L_{AL}$ (Full-SCDA) - $A_{AL}L_{\times L}$ (SCDA)

[m³/m³]

From 2014110100
To   2015103118
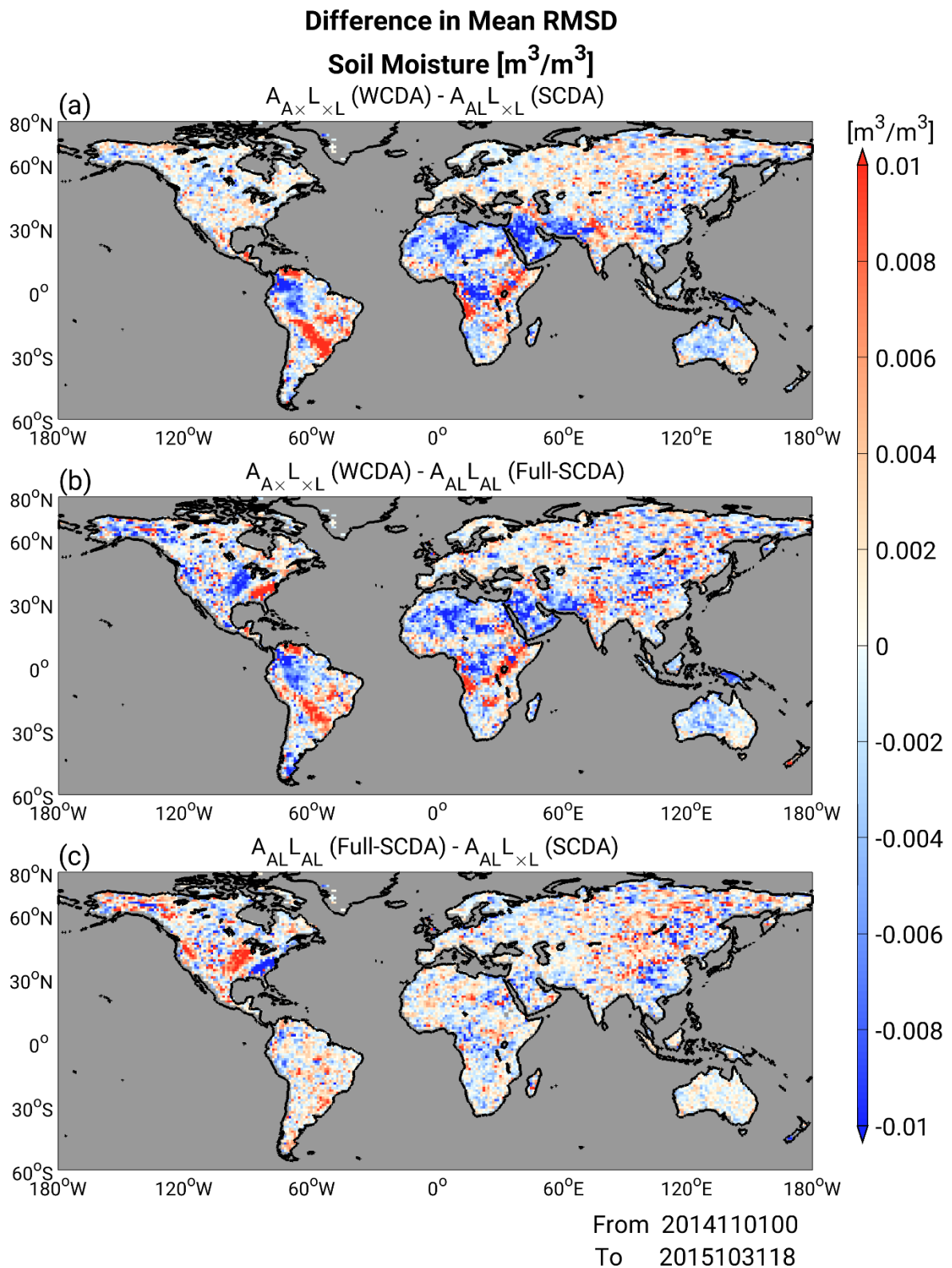
Figure 13. Similar to Fig. 7, but showing Global patterns of soil moisture analysis RMSD relative to ERA5 (m³ m⁻³).

 b. Impacts on atmospheric field

639   Here, we investigate the impacts of assimilation of SM on atmospheric variables. Fig.
640   14 shows the global patterns of forecast biases for temperature (K) in the lower troposphere
641   (850 hPa) relative to the ERA5 reanalysis data averaged over 12 months from November 2014
642   to October 2015. Hereafter, we discuss the results of $A_{A\times}L_{\times\times}$ (CTRL) and three coupled DA
643   experiments: $A_{A\times}L_{\times L}$ (WCDA), $A_{AL}L_{\times L}$ (SCDA), and $A_{AL}L_{AL}$ (Full-SCDA). Figure 14 (a)
644   shows that $A_{A\times}L_{\times\times}$ (CTRL) has a warm temperature bias in regions with dry SM biases, as
645   illustrated in Fig. 4 (e.g., South America, Africa, and Australia). In these regions, increasing
646   SM values after assimilation of SM decreases temperature estimates in the lower troposphere
647   (Figs. 14b−d), since more of the incoming solar and longwave radiation is converted to latent
648   heat flux, and less to sensible heat flux with greater SM. Compared to $A_{A\times}L_{\times L}$ (WCDA),
649   however, $A_{AL}L_{\times L}$ (SCDA) and $A_{AL}L_{AL}$ (Full-SCDA) show an overcooling effect for
650   temperature in the continents of Africa and Australia (Figs. 14c and d). This overcooling effect
651   is caused by the assimilation of SM into atmospheric variables in NICAM. The condition and
652   type of soil determine the allocation of energy to latent and sensible heat flux. In areas with
653   sufficient SM, evaporation is limited by the amount of available water, even though more
654   evaporation is energetically possible. In such a case, the ratio of latent heat to sensible heat (i.e.,
655   Bowen ratio) will be determined by the surface temperature. In contrast, in a dry area, the ratio
656   becomes smaller. In addition, the energy balance is led by the turbulent fluxes of sensible,
657   latent heat, and the ground heat flux. The energy transfer from the surface to the atmosphere
658   creates spatial pressure gradients that drive atmospheric circulation at various scales. Due to
659   the factors above, the most appropriate setting was $A_{A\times}L_{\times L}$ (WCDA) in our experiments. There
660   are no remarkable changes in temperature over the ocean among the DA methods.
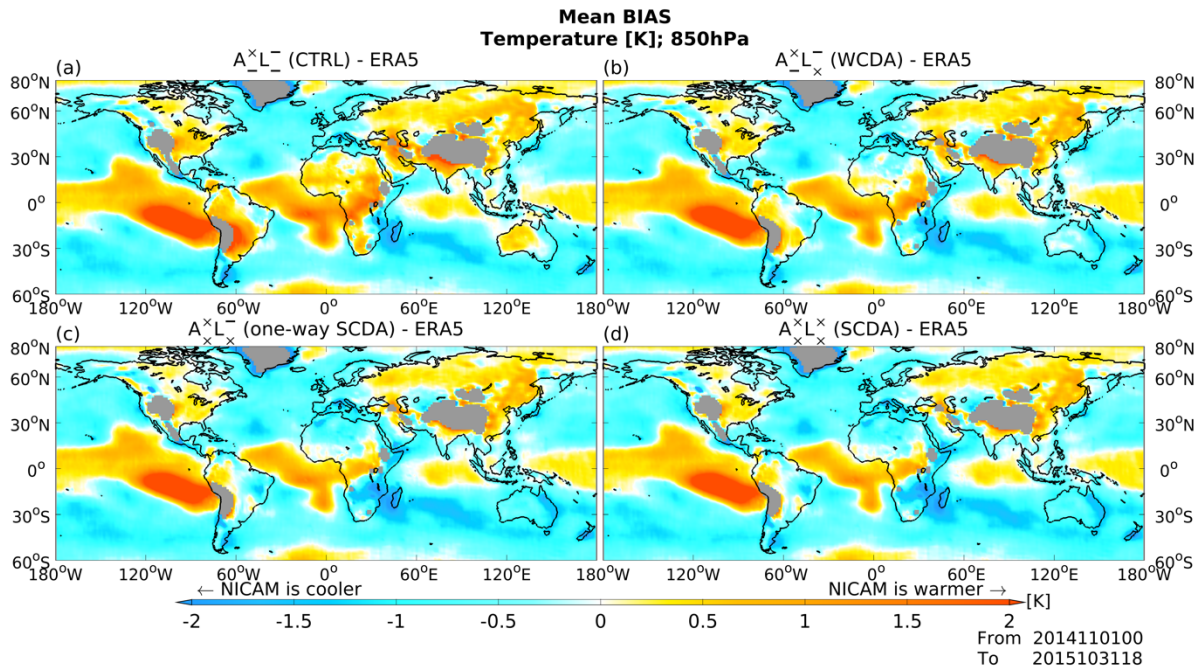
Figure 14. Global patterns of forecast bias for temperature (K) at 850 hPa relative to ERA5 reanalysis values for (a) $A_{A\times}L_{\times\times}$ (CTRL), (b) $A_{A\times}L_{\times L}$ (WCDA), (c) $A_{AL}L_{\times L}$ (SCDA), and (d) $A_{AL}L_{AL}$ (Full-SCDA), averaged over 12 months from November 2014 to October 2015. Red and blue colors represent warm and cold biases, respectively.

Table 1 summarizes the global-mean scores for bias, RMSD, and mean absolute difference (MAD) in temperature. Tables 1 (a) and (b) show these values averaged over the ocean and land, respectively. The errors in Table 1 (a) differ less strongly than those in Table 1 (b), showing that assimilation of SM changes the temperature field mainly over land. The bias values in Table 1 (b) show that $A_{A\times}L_{\times\times}$ (CTRL) has a warm temperature bias over land in general. Assimilating SM leads to a cooling effect, thereby mitigating the warm temperature bias. However, $A_{AL}L_{\times L}$ (SCDA) and $A_{AL}L_{AL}$ (Full-SCDA) decrease temperature too much, resulting in a cold bias. Consequently, $A_{A\times}L_{\times L}$ (WCDA) results in the best temperature field among the four experiments in terms of temperature bias at 850 hPa. Assimilating SM with $A_{A\times}L_{\times L}$ (WCDA) decreases the average temperature bias by 0.26 K over land. These changes over land do not propagate significantly to the temperature bias over the ocean.

680

Table 1. Averaged scores for bias, mean absolute difference (MAD), and RMSD for temperature at 850 hPa in Fig. 14. The biases and errors in (a) and (b) are averaged only over the ocean and only over land, respectively. The smallest errors are indicated by the bold font.

684

685   (a) over the ocean

Temperature [K]	(i) $A_{A\times}L_{\times\times}$ (CTRL)	(ii) $A_{A\times}L_{\times L}$ (WCDA)	(iii) $A_{AL}L_{\times L}$ (SCDA)	(iv) ¶ $A_{AL}L_{AL}$ (Full-SCDA)
BIAS	**-0.352**	-0.382	-0.434	-0.443
MAD	1.366	**1.363**	1.379	1.375
RMSD	1.590	**1.583**	1.600	1.595

686

687   (b) over land

Temperature [K]	(i) $A_{A\times}L_{\times\times}$ (CTRL)	(ii) $A_{A\times}L_{\times L}$ (WCDA)	(iii) $A_{AL}L_{\times L}$ (SCDA)	(iv) ¶ $A_{AL}L_{AL}$ (Full-SCDA)
BIAS	0.200	**-0.060**	-0.266	-0.268
MAD	1.320	**1.287**	1.326	1.334
RMSD	1.564	**1.510**	1.544	1.555

688

689

690

691

We also investigate changes in the precipitation field, focusing on the continent of Africa, where large changes in SM occurs due to SM DA (Fig. 4). Figures 15 (a)−(c) show the spatial patterns of analysis increments for precipitation amount, averaged over 12 months from November 2014 to October 2015. Note that DA can be used for analyzing not only model diagnosed variables (i.e., model state variables) but also other outputs from the model. For example, Kotsuki et al. (2017a) analyzed precipitation using NICAM-LETKF, where precipitation is not part of the initial condition. Here, we compare analysis increments of model-like precipitation (cf. Fig. 3 of Kotsuki et al., 2017a). Since precipitation is classified as an atmospheric diagnosed variable, we observe increments in precipitation during the assimilation of atmospheric observations. The difference in precipitation analysis increments between $A_{A\times}L_{\times\times}$ (CTRL) and $A_{A\times}L_{\times L}$ (WCDA) is insignificant (Figs. 15 a and b). In contrast, precipitation in $A_{AL}L_{\times L}$ (SCDA) can be affected by the assimilation of atmospheric and SM observations (Fig. 15 c). In central Africa, where precipitation amount changes significantly with SM DA, the analysis increments shift noticeably. We observe negative analysis increments where SM in $A_{A\times}L_{\times\times}$ (CTRL) is drier, and positive increments when it is wetter. This suggests that coupled land–atmospheric DA performs reasonably, as assimilating SM data increases (decreases) precipitation in areas where NICAM has a dry (wet) bias (Fig. 4a).

709
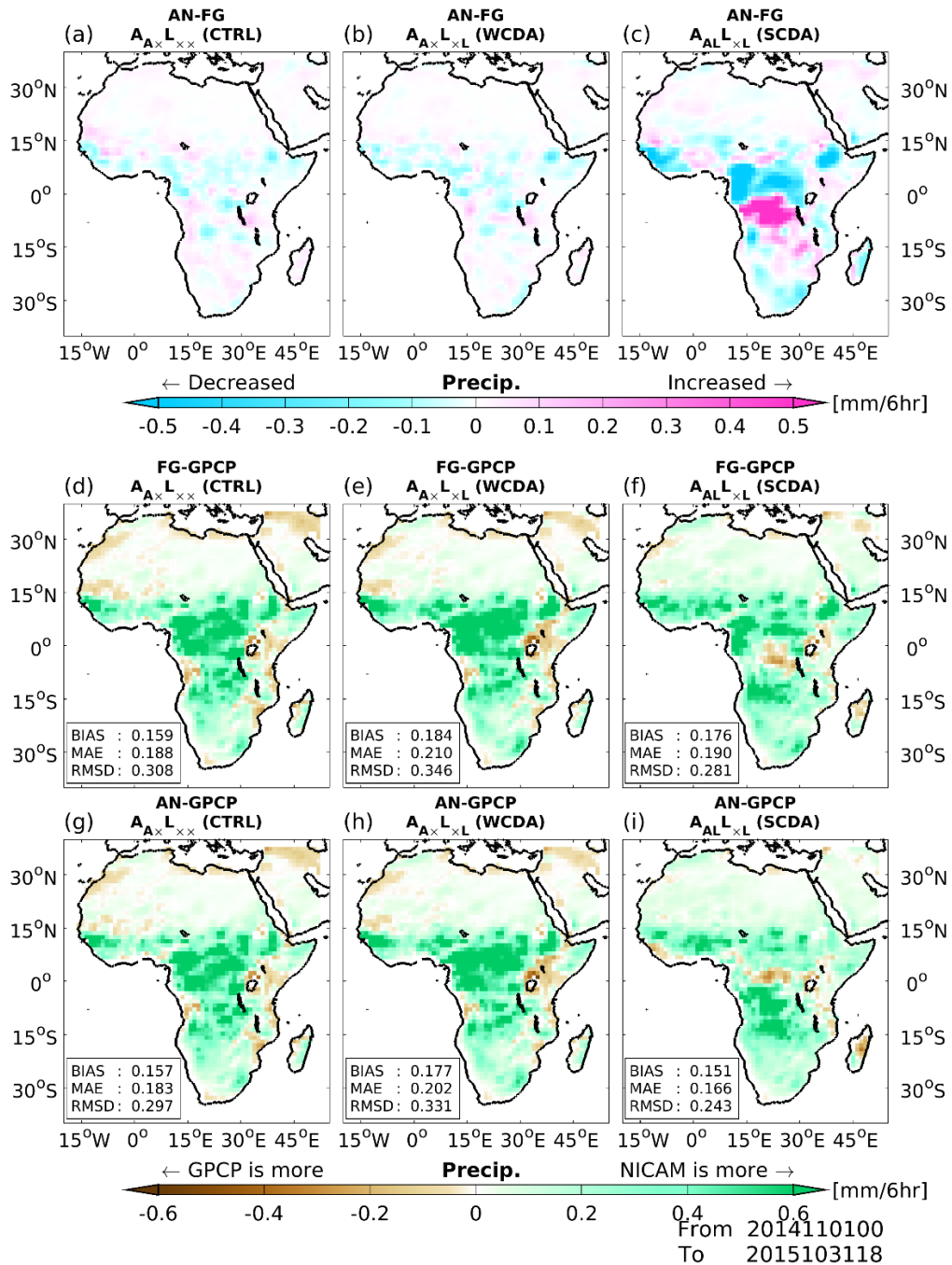
Figure 15. Spatial patterns of analysis increments for precipitation (mm 6h^{-1}; panels a–c), and precipitation forecast biases (panels d–f) and analysis biases (panels g–i) relative to GPCP version 1.3 (mm 6h^{-1}), averaged over 12 months from November 2014 to October 2015. Magenta and cyan colors in (a–c) represent increased and decreased precipitation with DA, respectively. The green and brown colors in (d–i) represent overestimated and underestimated precipitation values, respectively, relative to GPCP. Panels (a, d, g), (b, e, h), and (c, f, i) show the $A_{A\times}L_{\times\times}$ (CTRL), $A_{A\times}L_{\times L}$ (WCDA), and $A_{AL}L_{\times L}$ (SCDA) experiments, respectively.

717

File generated with AMS Word template 2.0

718   Spatial patterns of forecast and analysis biases in precipitation relative to GPCP version
719   1.3 estimates are shown in Figs. 15 (d)−(i). GPCP, which provides global precipitation data
720   through the merging of various satellite and gauge datasets, is considered to include the best
721   global precipitation estimates in the climate research community (Kotsuki et al., 2019c). First-
722   guess precipitation in $A_{A\times}L_{\times\times}$ (CTRL) has a positive bias relative to GPCP (Fig. 15d; +0.159
723   mm 6h^{-1}), and this overestimation is intensified in $A_{A\times}L_{\times L}$ (WCDA; +0.184 mm 6h^{-1}). In
724   contrast, the first-guess precipitation bias in $A_{AL}L_{\times L}$ (SCDA; +0.176 mm 6h^{-1}) is smaller than
725   that in $A_{A\times}L_{\times L}$ (WCDA), although both experiments assimilate SM (Figs. 15e and f). In
726     $A_{A\times}L_{\times\times}$ (CTRL) and $A_{A\times}L_{\times L}$ (WCDA), atmospheric variables are not updated through SM
727   DA. Therefore, differences between the precipitation biases of forecasting and analysis occur
728   due to assimilation of GSMaP_NRT in $A_{A\times}L_{\times\times}$ (CTRL) and $A_{A\times}L_{\times L}$ (WCDA). These two
729   experiments result in differing precipitation biases due to biases in their precipitation forecasts
730   (Figs. 15g and h). Assimilation of GSMaP_NRT slightly reduces the bias in precipitation
731   relative to GPCP (from 0.159 to 0.157 in $A_{A\times}L_{\times\times}$ (CTRL), and from 0.184 to 0.177 in $A_{A\times}L_{\times L}$
732   (WCDA). In contrast, SM DA changes the analysis precipitation in $A_{A\times}L_{\times L}$ (WCDA). $A_{AL}L_{\times L}$
733   (SCDA) shows the smallest bias in analysis precipitation. That is, updating atmospheric
734   variables with SM data plays an important role in improving the accuracy of precipitation.
735   Compared to $A_{A\times}L_{\times\times}$ (CTRL), one of the reasons for the larger bias in the $A_{A\times}L_{\times L}$ (WCDA)
736   and $A_{AL}L_{\times L}$ (SCDA) is due to increased rainfall in areas where NICAM has the dry bias.
737   Originally, NICAM overestimates precipitation (Kotsuki et al., 2019; Fig. 6). Improvements in
738   soil moisture may have reinforced the bias, which leads to worse scores in those cases. It can
739   be said that an improvement of the model bias contained in NICAM is necessary to solve this
740   problem.

741   Figure 16 compares the forecast biases in precipitation relative to GPCP averaged over
742   3 months from June to August 2015. We selected this period to explore SM-atmosphere
743   coupling, as suggested by Koster et al. (2004). Figure 16 (a) shows that NICAM tends to
744   overestimate precipitation in convergence regions at low latitudes (0°N−10°N) and
745   underestimate precipitation in South America and Southeast and East Asia. Figures 16 (b) and
746   (c) show changes in the precipitation forecasts of $A_{A\times}L_{\times L}$ (WCDA) and $A_{AL}L_{\times L}$ (SCDA). The
747   assimilation of SM affects precipitation mainly at low latitudes. As mentioned in Fig. 10,
748   Koster et al. (2004) found "hotspots" where SM affects precipitation during June−August.
749   Koster et al. (2004) noted that the initial condition of SM was sensitive to rainfall predictability

File generated with AMS Word template 2.0

750   over the North American Great Plains, equatorial Africa, and India (cf. Fig. 1 of Koster et al.,

751   2004). These areas correspond to the locations where forecast precipitation differed sharply

752   from SM DA, as shown in Figs. 16 (b) and (c), particularly for the Sahel, equatorial Africa,

753   and India. When comparing $A_{AL}L_{\times L}$ (SCDA) with $A_{A \times L}L_{\times L}$ (WCDA), coupled DA shows

754   stronger impacts in hotspots where the precipitation field is sensitive to the initial condition of

755   SM.

756

757

File generated with AMS Word template 2.0
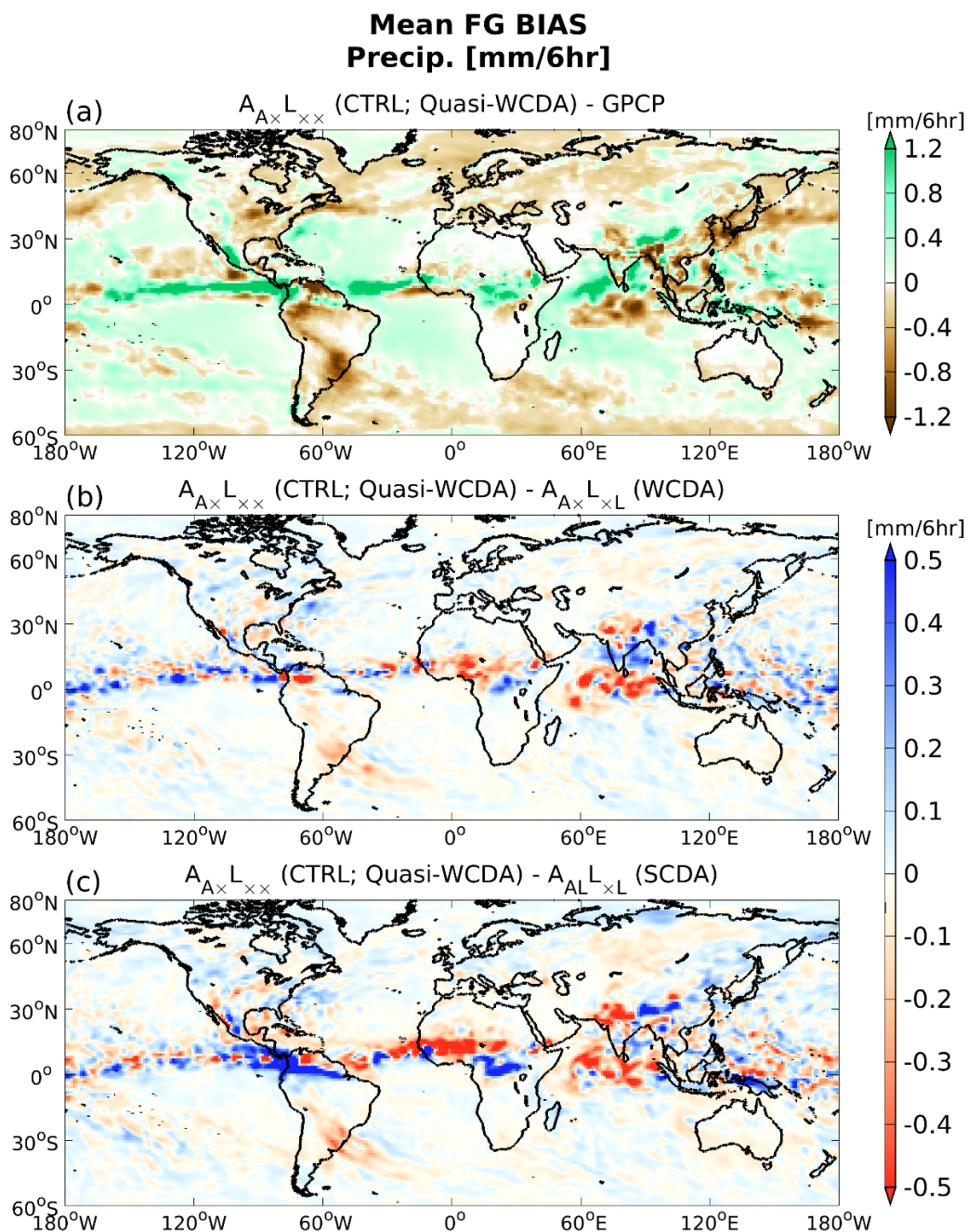
758   **Figure 16.** Spatial patterns of changes in precipitation (mm 6h^{-1}) averaged over 3 months

759 from June to August 2014. Panels (a), (b), and (c) show the difference between

760 $A_{A \times} L_{\times \times}$ (CTRL) and GPCP, $A_{A \times} L_{\times \times}$ (CTRL) and $A_{A \times} L_{\times L}$ (WCDA), and $A_{A \times} L_{\times \times}$ (CTRL)

761 and $A_{AL} L_{\times L}$ (SCDA), respectively. The green and brown colors in (a) represent overestimated

762 and underestimated precipitation values relative to GPCP, and the red and blue colors in (b, c)

763 represent increased and decreased precipitation values with SM DA, respectively.

764

765   Figure 17 shows vertical cross-sections of forecast biases for temperature and vapor

766 mixing ratio (Qv) relative to ERA5 reanalysis data along 20°E over the continent of Africa,

767 averaged over 12 months from November 2014 to October 2015. $A_{A \times} L_{\times \times}$ (CTRL) generally

768 shows a warm temperature bias and a dry humidity bias near the land surface (1000−800 hPa).

769 With the assimilation of SM, $A_{A \times} L_{\times L}$ (WCDA) and $A_{AL} L_{\times L}$ (SCDA) show decreases in

770 temperature of the lower troposphere at latitudes where $A_{A \times} L_{\times \times}$ (CTRL) has a warm bias (Figs.

771 17 b and c). Since the vertical layers of NICAM are almost the same as those of the ERA5, the

772 cooling impacts would not be attributed to the difference in vertical resolutions between

773 NICAM and ERA5. $A_{A \times} L_{\times L}$ (WCDA) propagates the impacts of SM DA for atmospheric

774 variables through the interaction between NICAM and MATSIRO during model time

775 integrations. In addition, $A_{AL} L_{\times L}$ (SCDA) updates atmospheric variables directly through SM

776 DA, which means $A_{AL} L_{\times L}$ (SCDA) alters atmospheric variables both directly and indirectly.

777 Therefore, $A_{AL} L_{\times L}$ (SCDA) lowers temperature too much due to the strong interaction between

778 SM and atmospheric variables (Fig. 17 c). Figure 17 (d) shows that most land surface areas

779 have dry Qv biases relative to the ERA5. This corresponds to the locations where

780 $A_{A \times} L_{\times \times}$ (CTRL) exhibits a moist bias against GLDAS (Fig. 4 a). As shown in Fig. 4, the

781 coupled DA improves this in those areas, which also leads to an enhancement in the Qv bias in

782 that region. As the moist bias relative to GLDAS in that area is improved through the SM DA,

783 the bias in Qv relative to ERA5 in that area is also improved by coupled assimilation. $A_{A \times} L_{\times L}$

784 (WCDA) and $A_{AL} L_{\times L}$ (SCDA) correct for the bias caused by increased or decreased Qv near

785 the surface using SM DA (Figs. 17 e and f). The change for Qv in $A_{AL} L_{\times L}$ (SCDA) is larger

786 than that in $A_{A \times} L_{\times L}$ (WCDA). This is because, as previously mentioned, $A_{AL} L_{\times L}$ (SCDA)

787 make larger adjustments to atmospheric variables compared to $A_{A \times} L_{\times L}$ (WCDA).

788
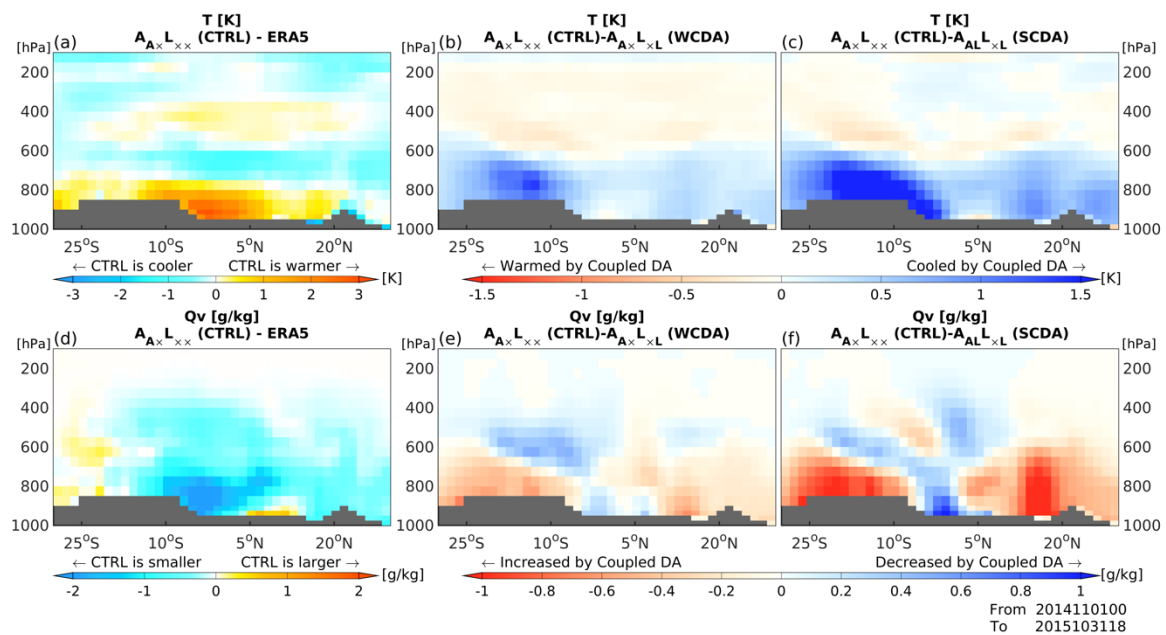
Figure 17. Vertical cross-sectional plots of differences in (a−c) temperature (K) and (d−f) water vapor mixing ratio (g kg⁻¹) averaged over 12 months from November 2014 to October 2015 along 20°E over the continent of Africa. Panels (a, d), (b, e), and (c, f) show the differences between $A_{A\times}L_{\times\times}$ (CTRL) and the ERA5 reanalysis, $A_{A\times}L_{\times\times}$ (CTRL) and $A_{A\times}L_{\times L}$ (WCDA), and $A_{A\times}L_{\times\times}$ (CTRL) and $A_{AL}L_{\times L}$ (SCDA), respectively. The vertical and horizontal axes show the pressure level from 1000 to 100 hPa and the latitude, respectively.

5. Conclusions

This study aims to explore the optimal coupled land–atmospheric DA method for improving weather forecasts through the assimilation of hydrological observations. We implement a coupled land–atmospheric DA into the NICAM-MATSIRO model and assimilated SM data from GLDAS. We perform a series of coupled DA experiments, including weakly and strongly coupled DA, and reach the following conclusions.

The assimilation of SM successfully mitigates SM biases. Updating SM by assimilating atmospheric observations can have detrimental impacts on SM, due to spurious error correlations between atmospheric observations and land model variables caused by insufficient ensemble size, and the difference in timescale between the atmospheric and land models. In contrast, updating the atmospheric model variables by assimilating SM observations has beneficial impacts on SM, implying that the error correlation between SM observations and

atmospheric model variables is more reliable. Consequently, the optimal coupled DA method in this study is $A_{AL}L_{\times L}$ (SCDA), in which atmospheric and SM data are used to update the atmospheric variables in NICAM, but only SM data are used to update the SM variable in MATSIRO. The results of this study indicate that $A_{AL}L_{AL}$ (Full-SCDA) is less effective than $A_{A\times}L_{\times L}$ (WCDA), which is caused by sampling errors and/or insufficient localization of the ensemble background-error covariance matrix. As Penny et al. (2019) have shown, experiments with a simple model to examine several factors in detail, such as the number of ensemble members, the scale of localization, the spread of the ensemble of initial members, and the frequency of coupling intervals, would yield very important information. With adequate settings, such as proposed by Penny et al. (2019), the experiments with $A_{AL}L_{AL}$ (Full-SCDA) might give a superior performance. In addition, the difference in dynamical timescales between the atmospheric and land models may possibly have a dominant influence. Using a shorter DA window with more linear cross-domain dynamics could be useful to investigate if this would help improve the impact of the $A_{AL}L_{AL}$ (Full-SCDA). This will be an important future study. Further, one possible reason why $A_{AL}L_{AL}$ (Full-SCDA) did not always show optimal results in the current study could be due to the poor and complex physical linkages between the lower troposphere and soil moisture. This problem has reasonably positive effects on the atmospheric field but often results in poor soil moisture analysis. The results presented in this study seem to indicate that this may be the case for $A_{AL}L_{AL}$ (Full-SCDA).

We demonstrate that precipitation and SM are closely related. Given the seasonal variation in precipitation distribution, the regions that would benefit from updating atmospheric variables using SM data shift accordingly. Assimilating SM provides a proper temperature estimation for the lower troposphere in areas with a dry SM bias and a warm atmospheric bias. This effect occurs because more incoming solar and longwave radiation was converted to latent heat flux and less converted to sensible heat flux with increased SM. However, assimilating SM into atmospheric model variables lead to overcooling effects in regions such as the continents of Africa and Australia. Furthermore, estimating precipitation based on SCDA is beneficial in Africa. Coupled DA has stronger impacts on precipitation forecasts in hotspots where the precipitation field is sensitive to the initial condition of SM.

This study demonstrates the potential for improving SM prediction using the NICAM-LETKF system by assimilating SM in strong coupled DA. SM is an important variable in land surface models, and its improvement can lead to better hydrological predictions such as

File generated with AMS Word template 2.0

841   droughts and floods. However, it is still unclear what atmospheric variables should be updated

842   using each land observation. Therefore, future studies will further investigate the effect of

843   variable localization for other land observations. When updating SM in MATSIRO with

844   atmospheric observations, we obtain unfavorable results due to errors in estimating the error

845   covariance between land model variables and atmospheric observations. The issue is thought

846   to be caused by experimental settings, rather than statistical aspects, due to the poor physical

847   relationships between the lower troposphere and SM. SM behavior is often highly localized

848   due to spatial differences such as soil texture, topography, and vegetation. Therefore, most

849   NWP centers use a point-wise analysis of SM, without considering the horizontal background

850   error covariance between grid points. The 40 ensemble members used in this study are close to

851   the number used in operational NWP centers, but using a larger number of ensembles could

852   lead to useful conclusions by evaluating the differences in performance between WCDA and

853   SCDA. Furthermore, using a large ensemble could be beneficial for understanding variable

854   localization more accurately by improving covariance estimation between components. In this

855   study, land observations are assimilated into the atmospheric model using the same vertical

856   localization scale as the assimilation of atmospheric observations. Using a smaller localization

857   scale in a limited ensemble size could help update atmospheric variables with SM assimilation

858   by reducing errors in the error covariance estimates. Furthermore, while this study uses SM

859   data based on GLDAS, assimilating satellite-derived SM data is an important direction for

860   future research. When actual GCOMW/AMSR-2 satellite observation data are assimilated, the

861   atmospheric field deteriorates significantly due to the assimilation of SM (not shown). This

862   suggests that limitations exist in the data assimilation method used in this study and that

863   technical measures, such as CDF matching preprocessing, may be necessary to assimilate

864   actual observation data successfully. Finally, it is found that resolution of about 100 km is very

865   coarse to simulate SM accurately. Note that the assimilation of GLDAS pseudo soil moisture

866   data is not a realistic operational setting, as it is likely to have much better spatial and temporal

867   coverage than real satellite observations. When actual observation data are assimilated at this

868   resolution, the representation error becomes large and can cause a problem. In addition to using

869   actual satellite observation data, using higher-resolution models is an important future

870   direction.

871

872

873   *Acknowledgments.*

874   K. Kurosawa and S. Kotsuki developed the experimental system for the parameter

875   estimation, conducted the experiments and analyzed the results. T. Miyoshi is the PI and

876   directed the research with substantial contribution to the development of this paper.

877   The authors thank the members of Data Assimilation Research Team, RIKEN Center

878   for Computational Science (R-CCS) and JAXA's PMM project. This study was partly

879   supported by JAXA Precipitation Measuring Mission (PMM), Advancement of meteorological

880   and global environmental predictions utilizing observational 'Big Data' of the social and

881   scientific priority issues (Theme 4) to be tackled by using post K computer of the

882   FLAGSHIP2020 Project of the Ministry of Education, Culture, Sports, Science and

883   Technology Japan (MEXT), the Initiative for Excellent Young Researchers of MEXT, JST AIP

884   Grant Number JPMJCR19U2, the Japan Society for the Promotion of Science (JSPS)

885   KAKENHI grant JP18H01549, JP21H04571, JP 21H05002 and JP22K18821, JST PRESTO

886   MJPR1924, and IAAR Research Support Program of Chiba University. The study used the

887   Supercomputer for earth Observation, Rockets, and Aeronautics (SORA) at JAXA, and the K

888   computer provided by the RIKEN R-CCS (Project IDs: ra000015, hp150289, hp160229,

889   hp170246, and hp180062).

890

891   *Data Availability Statement.*

892   The NICAM model code is available at http://www.nicam.jp/. The GSMaP precipitation

893   data is available at http://sharaku.eorc.jaxa.jp/GSMaP/. The NCEP PREPBUFR data is

894   available at http://rda.ucar.edu/datasets/ds337.0/. The GLDAS soil moisture data is available

895   at https://hydro1.gesdisc.eosdis.nasa.gov/data/GLDAS/. The GPCP precipitation data is

896   available at http://eagle1.umd.edu/GPCP_CDR/. The SMOS data is available at https://smos-

897   diss.eo.esa.int/oads/access. The GCOMW/AMSR-2 data is available at

898   https://lance.nsstc.nasa.gov/amsr2-science. The LETKF code developed in this study is based

899   on the open source code available at https://github.com/takemasa-miyoshi/letkf. All of the

900   data used in this study are stored for 5 years in Chiba University. Due to the large volume of

901   data and limited disk space, data will be shared online upon request (shunji.kotsuki@chiba-

902   u.jp; http://www.data-assimilation.riken.jp/index_e.html).

903

                                                APPENDIX

                                          Appendix A

906   This study diagnoses the observation error SD of SM by using innovation statistics

907   (Desroziers et al., 2005). The innovation statistics is given by:

908                    $(\sigma^o_{estimation})^2 = \langle (y^o - H\bar{x}^a)(y^o - H\bar{x}^f) \rangle,$ (A1)

909   where, σ^o is the observation error SD. Subscript *estimation* means the estimation by the

910   innovation statistics. The bracket $\langle \cdot \rangle$ denotes the statistical expectation. Here, we assumed the

911   observations error SD is globally constant and time independent for SM (Rodríguez-Fernández

912   et al., 2019). With NICAM-LETKF, we performed preliminary WCDA and SCDA

913   experiments over two months from October to November 2014, and used later one month

914   period data for the innovation statistics. Here we introduce a measure *factor,* given by

915                            $Factor = \sigma^o_{estimation}/\sigma^o_{prescribed},$ (A2)

916   where the subscript *prescribed* denotes the prescribed observation error SD of SM used in the

917   preliminary experiments. If the prescribed SD is optimal, then the diagnosed *factor* approaches

918   1.0. Table A1 summarizes the prescribed observation error SD and *factor* values for five

919   different observation SDs with assimilation of GLDAS SM. As noted by Ménard et al. (2009),

920   when the prescribed observation error SD is too small, the estimated observation error SD is

921   underestimated, whereas large SDs can lead to overestimation. Based on these preliminary

922   experiments, this study set the SM observation error SD at 0.05 (m^3 m^{-3}), which gave the *factor*

923   value closest to 1.0 among the preliminary experiments.

924

925   **Table A1**. Observation error SD diagnosed using innovative statistics. "Factor" is the ratio

926   of estimated error SD to the prescribed value (Eq. A2). The diagnostic values from $A^{\times}_{-}L^{-}_{\times}$

927   (WCDA) and $A^{\times}_{\times}L^{\times}_{\times}$ (SCDA) averaged over 2 months are shown.

928

929

Prescribed Obs.	Factor	
Error SD (m^3 m^{-3})	$A^{\times}_{-}L^{-}_{\times}$ (WCDA)	$A^{\times}_{\times}L^{\times}_{\times}$ (SCDA)

0.01	9.263	5.716
0.03	1.881	1.515
0.05	0.898	0.775
0.07	0.543	0.509
0.09	0.373	0.359

930

931

932

933

934

935

936

937

938

939

940

941 REFERENCES

942 Arakawa, A. and Schubert, W. H. (1974): Interaction of a Cumulus Cloud Ensemble with the
943   Large-Scale Environment, Part I. *J. Atmos. Sci.*, 31, 674–701. doi:10.1175/1520-
944   0469(1974)031<0674:IOACCE>2.0.CO;2.

945 Bateni, S. M., and Entekhabi, D. (2012): Relative efficiency of land surface energy balance
946   components. *Water Resour. Res.*, 48, W04510. doi:10.1029/2011WR011357.

947 Berry, E. (1967): Cloud Droplet Growth by Collection. *J. Atmos. Sci.*, 24, 688–701.
948   doi:10.1175/1520-0469(1967)024<0688:CDGBC>2.0.CO;2.

949   Betts, A. K. (2009): Land-Surface-Atmosphere Coupling in Observations and Models. *J. Adv.*
950   *Model. Earth Syst.*, 1, 4. doi:10.3894/JAMES.2009.1.4.

951   Bi, H., Ma, J., Zheng, W., and Zeng, J. (2016): Comparison of soil moisture in GLDAS model
952   simulations and in situ observations over the Tibetan Plateau. *J. Geophys. Res.*
953   *Atmos.*, 121, 2658– 2678. doi:10.1002/2015JD024131.

954   Bindlish, R., Cosh, MH., Jackson, TJ., Koike, T., Fujii, H., Chan, SK., Asanuma, J., Berg, AA.,
955   Bosch, DD., Caldwell, TG., Collins, CH., McNairn, H., Martinez-Fernandez, J., Prueger,
956   JH., Rowlandson, T. Seyfried, M. Starks, PJ. Thibeault, M. Van Der Velde, R. Walker,
957   JP. and Coopersmith, EJ. (2018): GCOM-W AMSR2 soil moisture product validation
958   using core validation sites. *IEEE Journal of selected topics in applied earth observations*
959   *and remote sensing*, vol. 11, no. 1, 8233417, pp. 209-219.
960   doi:10.1109/JSTARS.2017.2754293 doi: 10.1109/JSTARS.2017.2754293.

961   Bishop, C., Etherton, B., and Majumdar, S. (2001): Adaptive Sampling with the Ensemble
962   Transform Kalman Filter . Part I : Theoretical Aspects. *Mon. Wea. Rev.*, 129, 420–436.
963   doi: 10.1175/1520-0493(2001)129<0420:ASWTET>2.0.CO;2.

964   Bosilovich, M., Radakovich, J., Silva, A., Todling R., Verter, F. (2007): Skin Temperature
965   Analysis and Bias Correction in a Coupled Land-Atmosphere Data Assimilation System,
966   Journal of the Meteorological Society of Japan. Ser. II, Volume 85A, Pages 205-228,
967   Released on J-STAGE March 30, 2007.

968   Browne, P.A., de Rosnay, P., Zuo, H., Bennett, A., and Dawson, A. (2019): Weakly Coupled
969   Ocean–Atmosphere Data Assimilation in the ECMWF NWP System. Remote Sens. 11,
970   234. https://doi.org/10.3390/rs11030234

971   Hersbach, H, Bell, B, Berrisford, P, et al. (2020): The ERA5 global reanalysis. Q J R Meteorol
972   Soc. ; 146: 1999– 2049. https://doi.org/10.1002/qj.3803

973   Chen, F., Mitchell, K., Schaake, J., Xue, Y., Pan, H.-L., Koren, V., Duan, Q. Y., Ek, M.,
974   and Betts, A. (1996): Modeling of land surface evaporation by four schemes and
975   comparison with FIFE observations. *J. Geophys. Res.*, 101(D3), 7251–7268.
976   doi:10.1029/95JD02165.

977   Dee, D.P. (2005): Bias and data assimilation. *Q.J.R. Meteorol. Soc.*, 131: 3323-3343.
978   https://doi.org/10.1256/qj.05.137

979   De Lannoy, G. J. M., Reichle, R. H., Houser, P. R., Pauwels, V. R. N., and Verhoest, N. E. C.
980   (2007): Correcting for forecast bias in soil moisture assimilation with the ensemble
981   Kalman filter, Water Resour. Res., 43.

982   de Rosnay P, Drusch M, Vasiljevic D, Balsamo G, Albergel C, snf Isaksen L (2012): A
983   simplified extended Kalman filter for the global operational soil moisture analysis at
984   ECMWF. *Q J R Meteorol Soc*. doi:10.1002/qj.2023

985   de Rosnay, P., Balsamo, G., Albergel, C. et al. (2014): Initialisation of Land Surface Variables
986   for Numerical Weather Prediction. Surv Geophys 35, 607–621.

987   Desroziers G., Berre L., Chapnik B., and Poli P. (2005): Diagnosis of observation, background
988   and analysis-error statistics in observation space. *Q. J. R. Meteorol. Soc.*, 131, 3385–
989   3396. doi:10.1256/qj.05.108.

990   Dirmeyer, P.A. (2000): Using a Global Soil Wetness Dataset to Improve Seasonal Climate
991   Simulation. *J.   Climate,* 13, 2900–2922.   doi:10.1175/1520-
992   0442(2000)013<2900:UAGSWD>2.0.CO;2.

993   Dirmeyer, P.A. and S. Halder. (2016): Sensitivity of Numerical Weather Forecasts to Initial
994   Soil   Moisture   Variations   in   CFSv2. *Wea.   Forecasting,* 31, 1973–1983.
995   doi:10.1175/WAF-D-16-0049.1.

996   Douville, H. and Chauvin, F. (2000): Relevance of soil moisture for seasonal climate
997   prediction: A preliminary study. *Clim. Dyn.*, 16, 719–736. doi:10.1007/s003820000080.

998   Draper, C. and R.H. Reichle. (2019): Assimilation of Satellite Soil Moisture for Improved
999   Atmospheric Reanalyses. *Mon. Wea. Rev.,* 147, 2163–2188. doi:10.1175/MWR-D-18-
1000   0393.1.

1001 Draper, C. S. (2021): Accounting for Land Model Uncertainty in Numerical Weather
1002   Prediction Ensemble Systems: Toward Ensemble-Based Coupled Land–Atmosphere
1003   Data Assimilation, Journal of Hydrometeorology, 22(8), 2089-2104. Retrieved Oct 6,
1004   2022.

1005 Drusch, M. (2007): Initializing numerical weather prediction models with satellite-derived
1006   surface soil moisture: Data assimilation experiments with ECMWF's Integrated Forecast
1007   System and the TMI soil moisture data set. *J. Geophys. Res.*, 112, D03102.
1008   doi:10.1029/2006JD007478.

File generated with AMS Word template 2.0

Drusch, M. and P. Viterbo. (2007): Assimilation of Screen-Level Variables in ECMWF's Integrated Forecast System: A Study on the Impact on the Forecast Quality and Analyzed Soil Moisture. *Mon. Wea. Rev.,* 135, 300–314. doi:10.1175/MWR3309.1.

Evensen G. (2003): The Ensemble Kalman Filter: Theoretical formulation and practical implementation. *Ocean Dynamics*, 53, 343–367. doi:10.1007/s10236-003-0036-9.

Fairbairn, D., de Rosnay, P., and Browne, P. A. (2019): The New Stand-Alone Surface Analysis at ECMWF: Implications for Land–Atmosphere DA Coupling, *Journal of Hydrometeorology*, 20(10), 2023-2042.

Frolov, S., Bishop, C., Holt, T., Cummings, D., and Kuhl, D. (2016): Facilitating Strongly Coupled Ocean-Atmosphere Data Assimilation with an Interface Solver. *Monthly Weather Review*. 144. 150923131613008. 10.1175/MWR-D-15-0041.1.

Fujii, Y., Nakaegawa, T., Matsumoto, S., Yasuda, T., Yamanaka, G., and Kamachi, M. (2009): Coupled climate simulation by constraining ocean fields in a coupled model with ocean data. *J. Climate*, 22, 5541–5557. doi:10.1175/ 2009JCLI2814.1.

Gómez, B., Charlton-Pérez, CL., Lewis, H., and Candy, B. (2020): The Met Office Operational Soil Moisture Analysis System. Remote Sensing, 12(22):3691.

Hauser, M., Orth, R., and Seneviratne, S. I. (2017): Investigating soil moisture–climate interactions with prescribed soil moisture experiments: an assessment with the Community Earth System Model (version 1.2). *Geosci. Model Dev.*, 10, 1665-1677. doi:10.5194/gmd-10-1665-2017.

Honda, T., Miyoshi, T., Lien, G., Nishizawa, S., Yoshida, R., Adachi, S. A., Terasaki, K., Okamoto, K., Tomita, H., & Bessho, K. (2018): Assimilating All-Sky Himawari-8 Satellite Infrared Radiances: A Case of Typhoon Soudelor (2015), Monthly Weather Review, 146(1), 213-229.

Hoover, B. T., and Langland, R. H. (2017): Forecast and observation impact experiments in the Navy Global Environmental Model with assimilation of ECWMF analysis data in the global domain. *J. Meteor. Soc. Japan*, 95, 2017-023. doi:10.2151/jmsj.2017-023.

Hunt, B. R., Kostelich, E. J., and Szunyogh, I. (2007): Efficient data assimilation for spatiotemporal chaos: A local ensemble transform Kalman filter. *Physica D*, 230, 112–126. doi:10.1016/j.physd.2006.11.008.

1039   Kang, J.-S., E. Kalnay, J. Liu, I. Fung, T. Miyoshi, and K. Ide, 2011: ''Variable localization''
1040   in an ensemble Kalman filter: Application to the carbon cycle data assimilation. J.
1041   Geophys. Res., 116, D09110, https://doi.org/10.1029/2010JD014673.

1042   Kikuchi, K., Kodama, C., Nasuno, T., Nakano, M., Miura, H., Satoh, M., Noda, A. T., and
1043   Yamada, Y. (2017): Tropical intraseasonal oscillation simulated in an AMIP-type
1044   experiment by NICAM. *Climate Dyn.*, 48, 2507–2528. doi: 10.1007/s00382-016-3219.

1045   Kodama, C., Yamada, Y., Noda, A. T., Kikuchi, K., Kajikawa, Y., Nasuno, T., Tomita, T.,
1046   Yamaura, T., Takahashi, T. G., Hara, M., Kawatani, Y., Satoh, M., and Sugi, M. (2015):
1047   A 20-year climatology of a NICAM AMIP-type simulation. *J. Meteor. Soc. Japan*, 93,
1048   393–424. doi:10.2151/jmsj.2015-024.

1049   Koren, V., Schaake, J., Mitchell, K., Duan, Q. Y., Chen, F., and Baker, J. M. (1999): A
1050   parameterization of snowpack and frozen ground intended for NCEP weather and climate
1051   models. *J. Geophys. Res.*, 104, 19,569–19,585. doi:10.1029/1999JD900232.

1052   Koster, RD., Dirmeyer, PA., Guo, Z., Bonan, G., Chan, E., Cox, P., Gordon, CT., Kanae, S.,
1053   Kowalczyk, E., Lawrence, D., Liu, P., Lu, CH., Malyshev, S., McAvaney, B., Mitchell,
1054   K., Mocko, D., Oki, T., Oleson, K., Pitman, A., Sud, YC., Taylor, CM., Verseghy, D.,
1055   Vasic, R., Xue, Y., and Yamada, T. (2004): Regions of strong coupling between soil
1056   moisture and precipitation. *Science*, vol. 305, no. 5687, pp. 1138-1140.
1057   doi:10.1126/science.1100217.

1058   Kotsuki, S., Miyoshi, T., Terasaki, K., Lien, G.-Y., and Kalnay, E. (2017a): Assimilating the
1059   global satellite mapping of precipitation data with the Nonhydrostatic Icosahedral
1060   Atmospheric Model (NICAM). *J. Geophys. Res.*, 122, 631–650. doi:
1061   10.1002/2016JD025355.

1062   Kotsuki, S., Ota. Y., and Miyoshi, T. (2017b): Adaptive covariance relaxation methods for
1063   ensemble data assimilation: experiments in the real atmosphere. *Q. J. R. Meteorol. Soc.*,
1064   143, 2001–2015. doi: 10.1002/qj.3060.

1065   Kotsuki, S., Terasaki K., Yashiro H., Tomita H., Satoh M., and Miyoshi T. (2018): Online
1066   Model Parameter Estimation with Ensemble Data Assimilation in the Real Global
1067   Atmosphere: A Case with the Nonhydrostatic Icosahedral Atmospheric Model (NICAM)
1068   and the Global Satellite Mapping of Precipitation Data. *J. Geophys. Res.*, 123, 7375-
1069   7392. doi: 10.1029/2017JD028092.

1070 Kotsuki, S, Kurosawa, K, and Miyoshi, T. (2019a): On the properties of ensemble forecast
1071   sensitivity to observations. *Q J R Meteorol Soc.*, 1– 18. doi:10.1002/qj.3534.

1072 Kotsuki, S., Kurosawa, K., Otsuka, S., Terasaki, K., and Miyoshi, T. (2019b): Global
1073   Precipitation Forecasts by Merging Extrapolation-based Nowcast and Numerical
1074   Weather Prediction with Locally-optimized Weights. *Wea. and Forecasting*, 34, 701-
1075   714. doi:10.1175/WAF-D-18-0164.1.

1076 Kotsuki S., Terasaki K., Kanemaru K., Satoh M., Kubota T., and Miyoshi T. (2019c):
1077   Predictability of Record-Breaking Rainfall in Japan in July 2018: Ensemble Forecast
1078   Experiments with the Near-real-time Global Atmospheric Data Assimilation System
1079   NEXRA. *SOLA*, 15A, 1-7. doi: 10.2151/sola.15A-001

1080 Kumar, S.V., Peters-Lidard, C.D., Mocko, D., Reichle, R., Liu, Y., Arsenault, K.R., Xia, Y.,
1081   Ek, M., Riggs, G., Livneh, B., and Cosh, M. (2014): Assimilation of Remotely Sensed
1082   Soil Moisture and Snow Depth Retrievals for Drought Estimation. *J.
1083   Hydrometeor.,*15, 2446–2469. doi:10.1175/JHM-D-13-0132.1.

1084 Laloyaux, P., Balmaseda, M., Dee, D., Mogensen, K., and Janssen, P. (2016): A coupled data
1085   assimilation system for climate reanalysis. *Q.J.R. Meteorol. Soc.*, 142: 65-78.
1086   doi:10.1002/qj.2629.

1087 Lawless, A. (2012): Coupled model data assimilation. *Tech. Rep.*, p. 25, Int. Work. Coupled
1088   Data Assim. Univ. Reading, Reading, England.

1089 Lea, D.J., Mirouze, I., Martin, M.J., King, R.R., Hines, A., Walters, D., and Thurlow,
1090   M. (2015): Assessing a New Coupled Data Assimilation System Based on the Met Office
1091   Coupled Atmosphere–Land–Ocean–Sea Ice Model. *Mon. Wea. Rev.,* 143, 4678–
1092   4694. doi:10.1175/MWR-D-15-0174.1.

1093 Lin, L., and Pu, Z. (2019). Examining the Impact of SMAP Soil Moisture Retrievals on Short-
1094   Range Weather Prediction under Weakly and Strongly Coupled Data Assimilation with
1095   WRF-Noah, Monthly Weather Review, 147(12), 4345-4366.
1096   https://doi.org/10.1175/MWR-D-19-0017.1

1097 Lin, L., and Pu, Z. (2020). Improving Near-Surface Short-Range Weather Forecasts Using
1098   Strongly Coupled Land-Atmosphere Data Assimilation with GSI-EnKF, Monthly
1099   Weather Review, 148(7), 2863-2888. https://doi.org/10.1175/MWR-D-19-0370.1

File generated with AMS Word template 2.0

1100 Mahfouf, J., Viterbo P., Douville H., Beljaars A., and Saarinen S. (2000): A Revised land-
1101   surface analysis scheme in the Integrated Forecasting System. ECMWF Newsletter,
1102   Summer-Autumn

1103 Ménard, R., Yang, Y., and Rochon, Y. (2009): Convergence and stability ofestimated error
1104   variances derived from assimilation residuals in observa-tion space. *Proceedings of*
1105   *ECMWF Workshop on Diagnostics of DataAssimilation System Performance*, 15–17
1106   June 2009, Reading, UK.

1107 Miyoshi, T. and Yamane, S. (2007): Local Ensemble Transform Kalman Filtering with an
1108   AGCM at a T159/L48 Resolution. *Mon. Wea. Rev.*, 135, 3841–3861. doi:
1109   10.1175/2007MWR1873.1.

1110 Penny, S. and Hamill, T. (2017): Coupled Data Assimilation for Integrated Earth System
1111   Analysis and Prediction. *Bulletin of the American Meteorological Society*. 98.
1112   10.1175/BAMS-D-17-0036.1.

1113 Penny, S. G., Bach, E., Bhargava, K., Chang, C.-C., Da, C., Sun, L., and Yoshida, T. (2019):
1114   Strongly coupled data assimilation in multiscale media: Experiments using a quasi-
1115   geostrophic coupled model. *Journal of Advances in Modeling Earth Systems*, 11, 1803–
1116   1829.

1117 Penny, S.G., and Coauthors (2016): Coupled Data Assimilation for Integrated Earth System
1118   Analysis and Prediction: Goals, Challenges and Recommendations. WWRP 2017,
1119   https://repository.library.noaa.gov/view/noaa/28431

1120 Peters-Lidard, C. D., Kumar, S. V., Mocko, D. M., and Tian, Y. (2011): Estimating
1121   evapotranspiration with Land Data Assimilation Systems. *Hydrol. Processes*, 25, 3979–
1122   3992. doi:10.1002/hyp.8387.

1123 Reichle, R.H., McLaughlin, D.B., and Entekhabi, D. (2002): Hydrologic Data Assimilation
1124   with the Ensemble Kalman Filter. *Mon. Wea. Rev.,* 130, 103–114. doi:10.1175/1520-
1125   0493(2002)130<0103:HDAWTE>2.0.CO;2.

1126 Reichle, R. H., Koster, R. D., Liu, P., Mahanama, S. P., Njoku, E. G., and Owe, M. (2007):
1127   Comparison and assimilation of global soil moisture retrievals from the Advanced
1128   Microwave Scanning Radiometer for the Earth Observing System (AMSR-E) and the
1129   Scanning Multichannel Microwave Radiometer (SMMR). *J. Geophys. Res.*, 112,
1130   D09108. doi:10.1029/2006JD008033.

1131   Reichle, R. H., Kumar, S. V., Mahanama, S. P. P., Koster, R. D., Liu, Q. (2010): Assimilation
1132   of Satellite-Derived Skin Temperature Observations into Land Surface Models, Journal
1133   of Hydrometeorology, 11(5), 1103-1122.

1134   Rodell, M., Houser, P.R., Jambor, U., Gottschalck, J., Mitchell, K., Meng, C., Arsenault, K.,
1135   Cosgrove, B., Radakovich, J., Bosilovich, M., Entin, J.K., Walker, J.P., Lohmann, D.,
1136   and Toll, D. (2004): The Global Land Data Assimilation System. *Bull. Amer. Meteor.*
1137   *Soc.,* 85, 381–394. doi:10.1175/BAMS-85-3-381.

1138   Santanello, J.A., Lawston P., Kumar S., and Dennis E. (2019): Understanding the impacts of
1139   soil moisture initial conditions on NWP in the context of land–atmosphere coupling. *J.*
1140   *Hydrometeor.*, 20, 793–819, https://doi.org/10.1175/JHM-D-18-0186.1.

1141   Santanello, J.A., Kumar, S.V., Peters-Lidard, C.D., and Lawston, P.M. (2016): Impact of Soil
1142   Moisture Assimilation on Land Surface Model Spinup and Coupled Land–Atmosphere
1143   Prediction. *J. Hydrometeor.,* 17, 517–540. doi:10.1175/JHM-D-15-0072.1.

1144   Satoh, M., Matsuno, T., Tomita, H., Miura, H., Nasuno, T., and Iga, S. (2008): Nonhydrostatic
1145   icosahedral atmospheric model (NICAM) for global cloud resolving simulations. *J.*
1146   *Comput. Phys.*, 227, 3486–3514. doi: 10.1016/j.jcp.2007.02.006.

1147   Satoh, M., Tomita, H., Yashiro, H., Miura, H., Kodama, C., Seiki, T., Noda, A., Yamada, Y.,
1148   Goto, D., Sawada, M., Miyoshi, T., Niwa, Y., Hara, M., Ohno, Y., Iga, S., Arakawa, T.,
1149   Inoue, T., Kubokawa, H. (2014): The Non-hydrostatic Icosahedral Atmospheric Model:
1150   description and development. *Prog. Earth Planet. Sci.*, 1, 18. doi: 10.1186/s40645-014-
1151   0018-1.

1152   Sawada, Y., Nakaegawa, T., and Miyoshi, T. (2018): Hydrometeorology as an inversion
1153   problem: Can river discharge observations improve the atmosphere by ensemble data
1154   assimilation? *Journal of Geophysical Research:*
1155   *Atmospheres*, 123, 848– 860. doi:10.1002/2017JD027531.

1156   Sugiura, N., Awaji, T., Masuda, S., Mochizuki, T., Toyoda, T., Miyama, T., Igarashi, H.,
1157   and Ishikawa, Y. (2008): Development of a four-dimensional variational coupled data
1158   assimilation system for enhanced analysis and prediction of seasonal to interannual
1159   climate variations. *J. Geophys. Res.*, 113, C10017. doi:10.1029/2008JC004741.

1160 Suzuki, K., Zupanski, M., and Zupanski, D. (2017): A case study involving single observation
1161   experiments performed over snowy Siberia using a coupled atmosphere-land modelling
1162   system. *Atmos. Sci. Lett*, 18:106-111. doi:10.1002/asl.730.

1163 Sluka, T. C., Penny, S. G., Kalnay, E., and Miyoshi, T. (2016): Assimilating atmospheric
1164   observations into the ocean using strongly coupled ensemble data assimilation. *Geophys.*
1165   *Res. Lett.*, 43, 752–759. doi:10.1002/2015GL067238.

1166 Takata K., Emori S., and Watanabe T. (2003): Development of the minimal advanced
1167   treatments of surface interaction and runoff. *Global and Planetary Change*, 38, 209–222.
1168   doi:10.1016/S0921-8181(03)00030-4.

1169 Terasaki, K., Sawada, M., and Miyoshi, T. (2015): Local Ensemble Transform Kalman Filter
1170   Experiments with the Nonhydrostatic Icosahedral Atmospheric Model NICAM. *SOLA*,
1171   11, 23–26. doi: 10.2151/sola.2015-006.

1172 Terasaki, K., and Miyoshi, T. (2017): Assimilating AMSU-A Radiances with the NICAM-
1173   LETKF. *J. Meteorol. Soc. Japan*, 95, 433–446. doi: 10.2151/jmsj.2017-028.

1174 Terasaki, K., Kotsuki, S., and Miyoshi, T. (2019): Multi-year analysis using the NICAM-
1175   LETKF data assimilation system. *SOLA*, 15, 41–46. doi: 10.2151/sola.2019-009.

1176 Whitaker, J. S. and Hamill, T. M. (2012): Evaluating Methods to Account for System Errors in
1177   Ensemble Data Assimilation. *Mon. Wea. Rev.*, 140, 3078–3089. doi: 10.1175/MWR-D-
1178   11-00276.1.

1179 Zhang, S., Harrison, M.J., Rosati, A., and Wittenberg, A. (2007): System Design and
1180   Evaluation of Coupled Ensemble Data Assimilation for Global Oceanic Climate
1181   Studies. *Mon. Wea. Rev.,* 135, 3541–3564. doi:10.1175/MWR3466.1.